Inorg. Chem. **2003**, *42*, 1350−1365

Inorganic Chemistry
Article

Aqua Ions. 2. Structural Manifestations of the Jahn−Teller Effect in the *β*-Alums

Philip L. W. Tregenna-Piggott* and Hans-Peter Andres

Department of Chemistry and Biochemistry, University of Bern, Freiestrasse 3,
CH-3000, Bern 9, Switzerland

Garry J. McIntyre*

Institut Laue-Langevin, BP156, 38042 Grenoble, Cedex 9, France

Stephen P. Best

School of Chemistry, University of Melbourne, Parkville, Victoria 3010, Australia

Chick C. Wilson

ISIS Facility, Rutherford Appleton Laboratory, Chilton, Oxon, OX11 0QX, England

John A. Cowan

Institut Laue-Langevin, BP156, 38042 Grenoble, Cedex 9, France, and Chemistry Department,
University of Durham, South Road, Durham DH1 3LE, England

Received August 21, 2002

Variable-temperature single-crystal neutron diffraction structures of the alums $CsM^{III}(SO_4)_2 \cdot 12D_2O$, where M^{III} = Ti, V, Mn, and Ga, are reported. Structural differences are highlighted by the titanium and manganese alums, which undergo cubic ($Pa\bar{3}$) to orthorhombic (*Pbca*) phase transitions at ∼13 and ∼156 K, respectively. The structural instability exhibited by these salts is interpreted as arising from cooperative Jahn−Teller interactions, and these measurements characterize the structural changes that result from the coupling between the electronic and vibrational states. Although the symmetry changes associated with the phase transformations are analogous for the Ti and Mn alums, the low-temperature geometries of the tervalent hexaaqua cations are markedly different. Whereas the MnO_6 framework is subject to a pronounced tetragonal elongation, changes in the Ti−O bond lengths are very modest; but significant changes in the O−Ti−O bond angles and in the disposition of the coordinated water molecules are identified. The large differences in the transition temperatures and in the low-temperature stereochemistries of the $[Ti(OD_2)_6]^{3+}$ and $[Mn(OD_2)_6]^{3+}$ cations are related to the sensitivity of the energies of the t_{2g} (O_h) and e_g (O_h) orbitals to the various asymmetric vibrations of the hexaaqua complex.

1. Introduction

It is certainly not uncommon to profess oneself in structural manifestations of the Jahn−Teller effect.[1−9] The notion of tetragonally elongated octahedra is now so inculcated in the minds of chemists that to consider alternative distortion coordinates might seem profane. The following disquisition demonstrates that there is indeed life for the Jahn−Teller interaction, beyond coupling to the e_g asymmetric skeletal vibration. Structural data are presented for cesium sulfate alums, which exhibit varying degrees of structural instability; it is shown how variations in the structural chemistry can be related to the detailed electronic structure of the constituent ions.

---

* Authors to whom correspondence should be addressed. E-mail: tregenna@iac.unibe.ch (P.L.W.T.-P.); mcintyre@ill.fr (G.J.M.).

(1) Stebler, M.; Bürgi, H. B. *J. Am. Chem. Soc.* **1987**, *109*, 1395.

10.1021/ic0259639 CCC: $25.00

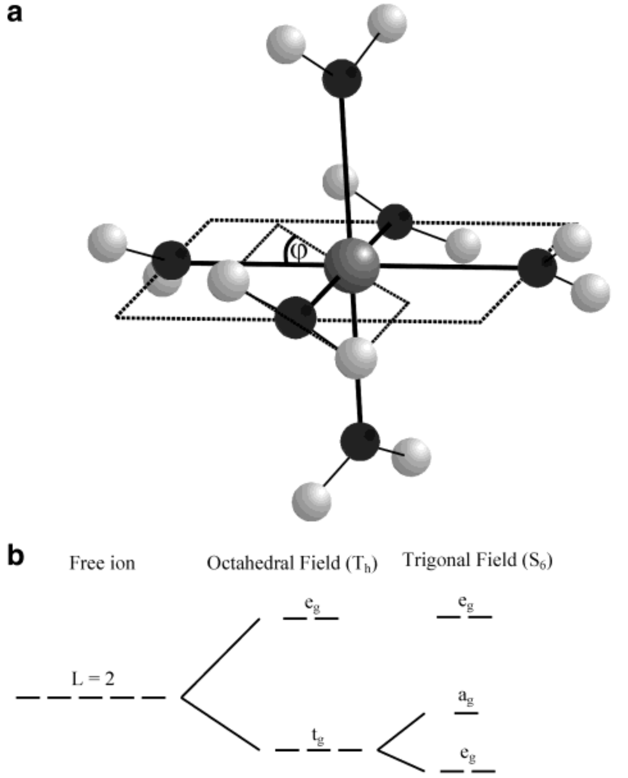

Figure 1. (a) Stereochemistry of the $[M(OH_2)_6]^{3+}$ cation in the cubic β alum lattice. (b) Splitting of the one-electron orbitals due to the cubic and trigonal fields.

Single-crystal neutron-diffraction data are reported for the Ti, V, Mn, and Ga cesium sulfate alums, which form part of a series of isomorphous salts, of formula $CsM^{III}(SO_4)_2 \cdot 12D_2O$ (CsMSD). A large number of tervalent cations can be accommodated in this crystal system, and all known salts crystallize in the cubic space group $Pa\bar{3}$, with the $[M(OH_2)_6]^{3+}$ cation on a site of S_6 symmetry.[10,11] With the exception of the salts formed by Co(III), Rh(III), and Ir(III), the cesium sulfate alums all crystallize in the β-modification, which may be identified by the stereochemistry of the $[M(OH_2)_6]^{3+}$ cation,[12] shown in Figure 1a. The MO_6 framework is close to a regular octahedron, and the mode of water coordination is trigonal planar. The trigonal distortion in this system is afforded primarily by a concomitant rotation of the water molecules about the $M^{III}-O$ bond vectors; the S_6 site symmetry results in a single unique water molecule, whose coordination geometry can be characterized by a twist angle, φ, defined in relation to the MO_6 framework.[13] From the wealth of experimental data for this system, in conjunction with angular overlap model (AOM) calculations,[13,14] a consistent picture of the splitting of the one-electron orbitals of the tervalent cation, resulting from the trigonal field, is obtained, and this is shown in Figure 1b. The ground terms predicted for the tervalent cations of interest to this study, both in cubic symmetry and in the S_6 symmetry imposed, are given in Table 1. The ground terms of Ti(III), V(III), Mn(III), and Ru(III) are orbitally degenerate in cubic symmetry, and structural manifestations of the Jahn−Teller effect could therefore be anticipated for the cesium sulfate alums formed from these ions. However, for the V(III) and Ru(III) alums, the Jahn−Teller effect is tempered by the trigonal field, which is substantial (~1940 and ~2500 cm^{-1} for V(III)[15,16] and Ru(III),[14] respectively) and gives rise to nondegenerate ground terms for these ions. To date, only the Cr,[13] Fe,[12] Ru,[17,18] and Mo[18] alums have been subject to single-crystal neutron-diffraction structural determinations, and these measurements have indeed revealed structural anomalies for the Ru(III) alum, principally in the value of φ, which is $-22.0(2)°$ for the Ru alum, and $-19.7(1)°$, $-19.0(4)°$, $-19.4(3)°$ for the Mo, Cr, and Fe alums, respectively. The larger magnitude of φ found for Ru(III) has been rationalized in terms of the tendency of the $[Ru(OD_2)_6]^{3+}$ cation to distort so as to maximize the stabilization of the ^2A_g term,[13] the value of φ being a compromise between the electronic preference of the $[Ru(OD_2)_6]^{3+}$ cation and hydrogen-bonding constraints of the lattice. The same considerations apply to the $[V(OD_2)_6]^{3+}$ cation, and the structural data presented in this study afford an interesting comparison with the Ru(III) data. The trigonal field does not lift the degeneracy of the ^5E_g ground term of Mn(III), and gives rise to a ^2E_g ground term for Ti(III). The neutron diffraction data presented here provide a precise characterization of the structural instability of the CsMnSD and CsTiSD alums, on account of the Jahn−Teller coupling interaction. The structural chemistry is shown to be strikingly different for the two alums, which may be related to the occupancy of the one-electron orbitals.

Table 1. Ground Terms Predicted for the Tervalent Cations of Interest to This Study, Both in Cubic Symmetry and in the S_6 Symmetry Imposed by the β-Alum Lattice

tervalent cation	ground term in T_h symmetry	ground term in the alum lattice (S_6 symmetry)
Ga	^1A_g	^1A_g
Cr	^4A_g	^4A_g
Mn	^5E_g	^5E_g
V	^3T_g	^3A_g
Fe	^6A_g	^6A_g
Ti	^2T_g	^2E_g
Ru	^2T_g	^2A_g
Mo	^4A_g	^4A_g

---

(2) Ammeter, J. H.; Bürgi, H. B.; Gamp, E.; Meyer-Sandrin, V.; Jensen, W. P. *Inorg. Chem.* **1979**, *18*, 733.

(3) Simmons, C. J.; Hitchman, M. A.; Stratemeier, H.; Schultz, A. J. *J. Am. Chem. Soc.* **1993**, *115*, 11304.

(4) Araya, M. A.; Cotton, F. A.; Daniels, L. M.; Falvello, L. R.; Murillo, C. A. *Inorg. Chem.* **1993**, *32*, 4853.

(5) Falvello, L. R. *J. Chem., Dalton Trans.* **1997**, 4463.

(6) Chen, Z.; Frei, S.; Strauss, H. L. *J. Am. Chem. Soc.* **1998**, *120*, 8789.

(7) Masters, V. M.; Riley, M. J.; Hitchman, M. A. *Inorg. Chem.* **2001**, *40* 843.

(8) Hitchman, M. A.; Maaskant, W.; van der Plas, J.; Simmons, C. J.; Stratemeier. *J. Am. Chem. Soc.* **2001**, *121*, 1488.

(9) Riley, M. J. *Top. Curr. Chem.* **2001**, *214*, 57.

(10) Beattie, J. K.; Best, S. P.; Skelton, B. W.; White, A. H. *J. Chem. Soc., Dalton Trans.* **1981**, 2105.

(11) Armstrong, R. S.; Beattie, J. K.; Best, S. P.; Skelton, B. W.; White, A. H. *J. Chem. Soc., Dalton Trans.* **1983**, 1973.

(12) Best, S. P.; Forsyth, J. B. *J. Chem. Soc., Dalton Trans.* **1990**, 395.

(13) Best, S. P.; Forsyth, J. B. *J. Chem. Soc., Dalton Trans.* **1991**, 1721.

(14) Daul, C.; Goursot, A. *Inorg. Chem.* **1985**, *24*, 3554.

(15) Best, S. P.; Clark, R. J. H. *Chem. Phys. Lett.* **1985**, *122* 401.

(16) Tregenna-Piggott, P. L. W.; Best, S. P. *Inorg. Chem.* **1996**, *35*, 5730.

(17) Best, S. P.; Forsyth, J. B. *J. Chem. Soc., Dalton Trans.* **1990**, 3507.

(18) Best, S. P.; Forsyth, J. B.; Tregenna-Piggott, P. L. W. *J. Chem. Soc., Dalton Trans.* **1993**, 2711.

2. Experimental Section

2.1. Synthesis. CsTiSH, CsVSH, and CsGaSH were synthesized by the addition of cesium sulfate to acidic solutions of titanium(III) sulfate, vanadium(III) chloride, and gallium(III) sulfate, respectively. The deuterated products were obtained by recrystallization (three times) from D_2SO_4 (1 M). Large single crystals were grown using a thermal gradient technique.[19] CsMnSD was prepared from a mixture of manganese(III) acetate, cesium sulfate, and D_2SO_4 (6 M) as previously described;[20] large single crystals were formed by allowing crystallization to take place at ca. 5 °C. The crystals selected for the neutron studies were all regularly octahedral, with dominant $\langle 1\ 1\ 1\rangle$ type faces.

2.2. Neutron Diffraction Measurements. Diffraction measurements were performed at the Institut Laue-Langevin, Grenoble, using either the four-circle diffractometer, D9 (CsMnSD and CsTiSD), or the Laue image-plate diffractometer, LADI (CsVSD); and at the ISIS facility at the Rutherford Appleton Laboratories using the Laue time-of-flight diffractometer SXD (CsTiSD, CsGaSD, CsVSD). The fractional coordinates obtained from the SXD measurements on CsTiSD and CsVSD were in good agreement with those obtained on the D9 and LADI instruments, but the estimated standard deviations (esds) of the fractional coordinates were somewhat poorer. These structures are included as Supporting Information.

2.2.1. D9 Structures of CsTiSD and CsMnSD. Neutron-diffraction data for CsMnSD and CsTiSD were obtained at wavelengths of 0.8412(1) (CsMnSD) and 0.8465(2) Å (CsTiSD). The samples were mounted in a He-flow cryostat[21] allowing temperatures down to 2 K to be reached without loss of four-circle access. D9 is also equipped with a small two-dimensional area detector[22] which for these measurements allows optimal delineation of the peak from the background, and observation of possible spread in three dimensions in the reflections due to twinning at the cubic-to-orthorhombic transition. For all data, background and Lorentz corrections were applied.[23] For both compounds the regular crystal morphology results in approximately equal absorption for all reflections of each compound; therefore no absorption corrections were deemed necessary.

Structure refinements were made using programs based on the Cambridge Crystallographic Subroutine Library.[24] Initial refinements showed that extinction affected only a few reflections of each compound, and could be well accounted for by a Becker & Coppens[25,26] type-I model[25] with a Lorentzian distribution of mosaic blocks. The low degree of extinction and the regular form of the crystal meant that the data at each temperature could be averaged over symmetry-equivalent reflections. For CsMnSD $y_{\min} = 0.69$ for the 0 4 0, and all but 2% of the data have $y \geq 0.95$ at 170 K; at 5 K, where twinning reduces the coherence length, $y = 0.89$ for the 0 4 0.

2.2.2. SXD Structures of CsTiSD, CsGaSD, and CsVSD. Large single crystals of approximate dimension 3.5 × 3.5 × 3.5 mm^3 were mounted in a closed-cycle refrigerator, mounted on either a (ϕ, χ) orienter (CsGaSD) or an ω-rotation stage (CsTiSD, CsVSD) of SXD.[27,28] This method uses a wavelength-sorted white neutron beam, along with large-area position-sensitive detectors, to allow a large volume of reciprocal space to be measured in a single crystal setting (a “frame”). For the CsGaSD sample a total of 28 frames (300 μA·h of integrated proton current from the source, ca. 2 h exposure time) were collected at a range of ϕ, χ values. A total of 12 and 10 frames (500 μA·h of integrated proton current from the source, ca. 3 h exposure time) were collected for CsTiSD and CsVSD, respectively. For all samples the temperature stability, as measured by a Rh−Fe sensor close to the sample, was better than ±1 K throughout. The reflection intensities were extracted and reduced to structure factors using standard procedures.[28]

2.2.3. LADI Structure of CsVSD. The white-beam Laue diffractometer, LADI, is essentially a cylindrical image-plate detector which subtends 63% of the full solid angle at the crystal.[29,30] Normally this instrument is used for macromolecular crystallography and is located on a long-wavelength cold-neutron beam. In these experiments LADI was installed on a thermal-neutron guide with usable wavelengths from 0.8 to 4.5 Å, where it has been shown to give a 10-fold gain in efficiency in crystallographic investigation of small-unit-cell materials.[31] Diffraction data were obtained for CsVSD during one such trial period. The 8 mm^3 crystal was mounted on the cold head of an Edwards cryorefrigerator regulated for the measurements at 15 K. Four Laue diffraction patterns were obtained with the crystal bathed in the unmonochromated thermal neutron beam and rotated 25° around the (vertical) axis of the cylinder between the 45 min exposures.

The Laue diffraction patterns were indexed using the Lauegen program[32,33] and the reflections integrated using a two-dimensional version of the $\sigma(I)/I$ algorithm.[34] The reflections were normalized to the same incident wavelength by the program Lauenorm,[35] which derives an empirical scaling curve as a function of wavelength by comparison over all patterns of multiple observations and equivalent reflections. Only data in the wavelength band 1.1−1.9 Å, with crystal d spacing $\geq$ 0.8 Å, were accepted, since reflections recorded outside this range were of very low intensity, or very few in number. Data with $I < \sigma(I)/2$ were also rejected. Each diffraction pattern contributed on average 1292 independent observations of which 708 were unique. The total number of unique observations over all four patterns was 1032, some 77% of all unique reflections for d spacing > 0.8 Å. Because of the regular form of the crystal, the attenuation due to absorption will be approximately equal for all reflections observed at the same wavelength, and the wavelength dependence of the absorption is corrected by an empirical normalization; therefore, no explicit correction for absorption was made. Structure refinements were again made using programs based on the Cambridge Crystallographic Subroutine Library.[24] It was evident

---

(19) Best, S. P.; Beattie, J. K.; Armstrong, R. S. *J. Chem. Soc., Dalton Trans.* **1984**, 2611.
(20) Christensen, O. T. *Z. Anorg. Chem.* **1901**, *27*, 329.
(21) Zeyen, C. M. E.; Chagnon, R.; Disdier, F.; Morin, H. *Rev. Phys. Appl.* **1984**, *19*, 789.
(22) Lehmann, M. S.; Kuhs, W.; Allibon, J.; Wilkinson, C.; McIntyre, G. J. *J. Appl. Crystallogr.* **1989**, *22*, 562.
(23) Wilkinson, C.; Khamis, H. W.; Stansfield, R. F. D.; McIntyre, G. J. *J. Appl. Crystallogr.* **1988**, *21*, 471.
(24) Matthewman, J. C.; Thompson, P.; Brown, P. J. *J. Appl. Crystallogr.* **1982**, *15*, 167.
(25) Becker, P.; Coppens, P. *Acta Crystallogr.* **1974**, *A30*, 129.
(26) Becker, P.; Coppens, P. *Acta Crystallogr.* **1975**, *A31*, 417.
(27) Wilson, C. C. In *Neutron Scattering Data Analysis*; Johnson, M. W., Ed.; IoP Conference Series 107; Adam Hilger: Bristol, 1990; p 145.
(28) Wilson, C. C. *J. Mol. Struct.* **1997**, *405*, 207.
(29) Wilkinson, C.; Lehmann, M. S. *Nucl. Instrum. Methods Phys. Res., Sect. A* **1991**, *310*, 411.
(30) Cipriani, F.; Castagna, J.-C.; Lehmann, M. S.; Wilkinson, C. *Physica B* **1995**, *213/214*, 975.
(31) Cole, J. M.; McIntyre, G. J.; Lehmann, M. S.; Myles, D. A. A.; Wilkinson, C.; Howard, J. A. K. *Acta Crystallogr.* **2001**, *A57*, 429.
(32) Campbell, J. W. *J. Appl. Crystallogr.* **1995**, *28*, 228.
(33) Campbell, J. W.; Hao, Q.; Harding, M. M.; Nguti, N. D.; Wilkinson, C. *J. Appl. Crystallogr.* **1998**, *31*, 496.
(34) Wilkinson, C.; Khamis, K. H.; Stansfield, R. F. D.; McIntyre, G. J. *J. Appl. Crystallogr.* **1988**, *21*, 471.
(35) Campbell, J. W.; Habash, J.; Helliwell, J. R.; Moffat, K. Determination of the wavelength normalisation curve in the Laue method. *Q. Protein Crystallogr.* **1986**, *18*.

Table 2. Data Collection and Analysis Parameters for Measurements Performed on the Four-Circle Single-Crystal Neutron Diffractometer D9[a]

		Crystal Data		
chem formula	$CsMn(SO_4)_2\cdot 12D_2O$	$CsMn(SO_4)_2\cdot 12D_2O$	$CsTi(SO_4)_2\cdot 12D_2O$	$CsTi(SO_4)_2\cdot 12D_2O$
chem fw (g)	620	620	613	613
temp (K)	170	5	20	2
cell setting	cubic	orthorhombic	cubic	orthorhombic
space group	$Pa\bar{3}$	*Pbca*	$Pa\bar{3}$	*Pbca*
a (Å)	12.4213(6)	12.3680(10)	12.4091(6)	12.42636(2)
b (Å)		12.4803(10)		12.39479(2)
c (Å)		12.3117(8)		12.38068(2)
V (Å^3)	1916.5(2)	1900.4(3)		1906.899(2)
wavelength (Å)	0.8412(1)	0.8412(1)	0.8465(2)	0.8465(2)
Z	4	4	4	4
no. of reflns for cell params	655	1034	1049	cell params from HRPD
θ range (deg)	5−40	5−47	4−45	
μ (mm^{-1})	0.015	0.015	0.014	0.014
cryst form	octahedron	octahedron	octahedron	octahedron
cryst size (mm^3)	13.1	13.1	8.9	8.9
cryst color	deep purple	deep purple	deep red	deep red
data-collection meth	$\omega - x\theta$ scans	$\omega - x\theta$ scans	$\omega - x\theta$ scans	$\omega - x\theta$ scans
no. of measd reflns	2231	3885	2397	3794
no. of indep reflns	1147	3599	1478	3473
R_{int}	0.053	0.017	0.026	0.027
θ_{max} (deg)	47	48	45	45
range of *h*, *k*, *l*	$-14 \le h \le 8$ $0 \le k \le 21$ $-8 \le l \le 21$	$-21 \le h \le 20$ $-4 \le k \le 20$ $-18 \le l \le 21$	$-3 \le h \le 18$ $-3 \le k \le 14$ $-14 \le l \le 0$	$-14 \le h \le 20$ $-13 \le k \le 20$ $-20 \le l \le 6$
no. of standard reflns	1	1	1	1
freq of standard reflns	every 50 reflns	every 50 reflns	every 30 reflns	every 50 reflns
		Refinement		
refinement on	*F*	*F*	*F*	*F*
R(*F*)	0.101	0.062	0.034	0.041
$R_w(F)$	0.044	0.047	0.025	0.035
S	2.03	2.22	2.79	6.32
no. of reflns used in refinement	1147	3599	1366	3473
no. of params used	74	158	73	158
weighting scheme (all data)	$w = 1/[\max(\sigma^2(F_o^2),\sigma_{pop}(F_o^2))]$			
extinction method (all data)	Lorentzian type 1 isotropic (Becker & Coppens, 1974, 1975)			
extinction coeff (10^{-4} rad^{-1})	1.11(5)	0.237(1)	0.44(1)	0.2300(1)
source of atomic scattering factors (all data)	Sears (1986)			
		Computer Programs		
data collection (all data)	MAD (Barthélemy, 1984)			
cell refinement (all data)	RAFD9 (Filhol, 1987)			
data reduction (all data)	RACER (Wilkinson et al., 1988) CCSL (Matthewman et al.)			
structure refinement (all data)	SFLSQ (based on CCSL)			

[a] The 2 K cell parameters of $CsTi(SO_4)_2\cdot 12D_2O$ were taken from an earlier HRPD study (high-resolution powder neutron diffraction).[36]

in the first refinements that the observed intensities of the strongest reflections were reduced by extinction. The final refinement was therefore made against the unmerged normalized data with the wavelength of the individual observations included in the Becker & Coppens type-I model for secondary extinction.[25]

3. Results

3.1.1. Structural Data of CsMnSD and CsTiSD. Prior to the measurements reported in the present work, a variable-temperature powder neutron diffraction study of CsTiSD characterized a ∼13 K cubic to orthorhombic phase transition,[36] and a corresponding powder X-ray diffraction study of CsMnSD suggested an analogous phase transition at ∼160 K. Thus the strategy for the data collection of CsTiSD and CsMnSD first involved structural determinations in the cubic phases; then, characterization of the phase transitions by monitoring the intensities of certain reflections through the phase transitions; and finally, collection of comprehensive data sets at temperatures well below the phase transitions.

170 K Structural Determination of CsMnSD. The data collection and analysis parameters for the high-temperature cubic structure of CsMnSD are summarized in Table 2. Averaging the 2231 measured reflections yielded 1147 unique reflections with an internal agreement index of 5.3%. The unit cell dimensions were obtained from the UB matrix generated by the program RETREAT. The UB matrix was calculated using the centroids of the 655 strongest reflections covering the full range of sin θ/λ. The weighted least-squares refinement gave a final *R* factor of 0.101, weighted *R* factor of 0.044, and χ^2 of 2.03 for the 1147 observables with a total of 74 variables comprising 23 positional parameters, two isotropic thermal parameters for Cs and Mn, 46 anisotropic thermal parameters for the remaining atoms, two scaling parameters, and a single parameter to describe the crystalline mosaic spread in the Becker−Coppens model for extinction. Selected interatomic distances and bond angles,

---

(36) Tregenna-Piggott, P. L. W.; Best, S. P.; O'Brien, M. C. M.; Knight, K. S.; Forsyth, J. B.; Pilbrow, J. R. *J. Am. Chem. Soc.* **1997**, *119*, 3324.

Table 3. Bond Lengths (Å) and Angles (deg) Which Define the Coordination Environment of the Mn(III) Cation at 170 and 5 K, and the Ti(III) Cation at 20 and 2 K[a]

	cubic phases			orthorhombic phases	
	CsMnSD 170 K	CsTiSD 20 K		CsMnSD 5 K	CsTiSD 2 K
			(i) $[M(OD_2)_6]^{3+}$		
M−O(b)	1.988(1)	2.037(1)	M−O(d)	1.929(1)	2.036(2)
			M−O(e)	2.129(2)	2.030(2)
			M−O(f)	1.924(1)	2.043(2)
O(b)−M−O(b)	91.00(7)	90.37(2)	O(d)−M−O(e)	91.31(5)	91.08(9)
			O(d)−M−O(f)	90.69(5)	89.30(12)
			O(e)−M−O(f)	90.92(6)	90.70(9)
tilt M−OD_2(b)	−0.1(3)	0.3(1)	tilt M−OD_2(d)	−0.9(3)	1.9(4)
			tilt M−OD_2(e)	4.2(3)	−4.9(4)
			tilt M−OD_2(f)	−1.7(3)	2.6(4)
ψ M−OD_2(b)	64.7(3)	65.6(1)	ψ M−OD_2(d)	65.3(3)	64.1(4)
			ψ M−OD_2(e)	64.4(3)	66.3(4)
			ψ M−OD_2(f)	64.4(3)	66.5(4)
			(ii) Water Molecules		
O(b)−D(b1)	1.005(2)	1.001(1)	O(d)−D(d1)	1.015(2)	0.999(4)
O(b)−D(b2)	0.987(2)	0.986(1)	O(d)−D(d2)	0.996(2)	0.987(4)
			O(e)−D(e1)	0.990(2)	1.001(3)
			O(e)−D(e2)	0.977(2)	0.987(3)
			O(f)−D(f1)	1.016(2)	1.006(4)
			O(f)−D(f2)	0.994(2)	0.989(4)
D(b1)−O(b)−D(b2)	110.8(2)	109.61(8)	D(d1)−O(d)−D(d2)	111.8(2)	109.5(3)
			D(e1)−O(e)−D(e2)	108.7(2)	110.3(3)
			D(f1)−O(f)−D(f2)	111.0(2)	109.0(4)
			(iii) Hydrogen Bonds		
D(b2)···O(2)	1.667(2)	1.648(1)	D(d2)···O(S2)	1.637(2)	1.647(3)
			D(e2)···O(S3)	1.731(2)	1.664(3)
			D(f2)···O(S4)	1.638(2)	1.667(4)
D(b1)···O(a)	1.601(2)	1.613(1)	D(d1)···O(c)	1.556(2)	1.604(3)
			D(e1)···O(a)	1.686(2)	1.603(3)
			D(f1)···O(b)	1.562(2)	1.619(4)
O(b)−O(a)	2.604(2)	2.613(1)	O(d)−O(c)	2.569(2)	2.602(3)
			O(e)−O(a)	2.674(2)	2.602(3)
			O(f)−O(b)	2.576(2)	2.624(4)
O(b)···D(b1)−O(a)	176.4 (2)	176.75 (7)	O(d)···D(d1)−O(c)	175.6(2)	178.4(3)
			O(e)···D(e1)−O(a)	176.5(2)	174.9(3)
			O(f)···D(f1)−O(b)	176.1(2)	176.6(3)
O(b)−O(2)	2.655(2)	2.648(1)	O(d)−O(S2)	2.632(2)	2.634(3)
			O(e)−O(S3)	2.708(2)	2.652(3)
			O(f)−O(S4)	2.632(2)	2.655(3)
O(b)···D(b2)−O(2)	178.8 (2)	178.88 (7)	O(d)···D(d2)−O(S2)	178.3(2)	178.3(3)
			O(e)···D(e2)−O(S3)	178.5(2)	179.3(3)
			O(f)···D(f2)−O(S4)	178.1(2)	177.5(3)

[a] A more extensive tabulation may be found in Supporting Information. The tilt angle is the defined as the angle between the M−O bond vector and the water plane. The AOM twist angle, ψ, is formally defined in ref 54.

which define the coordination environment about the manganese(III) cation, are listed in Table 3. The fractional cell coordinates and thermal parameters are included as Supporting Information as is a more extensive tabulation of structural parameters.

Phase Transition of CsMnSD. The phase transition of CsMsSD is most clearly manifested in the diffraction experiments by a discontinuity in the temperature dependence of the intensities of the Bragg reflections. The temperature dependence of the intensities of two such reflections, obtained by slowly cooling the crystal below 170 K, is shown in Figure 2. Both reflections show a discontinuous increase in intensity at 156 K, indicative of a first-order transition. The data suggest that no further phase transitions occur below 156 K. Whereas both reflections are slightly broader below the transition temperature, there is no clear splitting of the reflections even at 5 K.

5 K Structural Determination of CsMnSD. Since the lengths of the unit cell axes in the high- and low-temperature phases are similar, the phase transition from $Pa\bar{3}$ to *Pbca* may result in retention of a cubic diffraction pattern if the resulting crystal has approximately equally populated domains aligned along the *x*, *y*, and *z* axes. The observation that the positions of the reflections from the crystal at 5 K were much better predicted by an orthorhombic than by a cubic lattice implies that there is unequal population of the three domains, possibly as the result of uniaxial strain associated with attachment of the crystal to the mounting pin. The 5 K data were refined using a model that allowed for three domains, related by the cubic 3-fold axis (eq 1):

$$|F_o| = \sqrt{[p_1F_c^{\,2}(hkl) + p_2F_c^{\,2}(klh) + p_3F_c^{\,2}(lhk)]} \qquad (1)$$

with $p_1 + p_2 + p_3 = 1$. The domain populations refined to values of 0.878(3):0.094(2):0.028(2). The unit cell dimen-

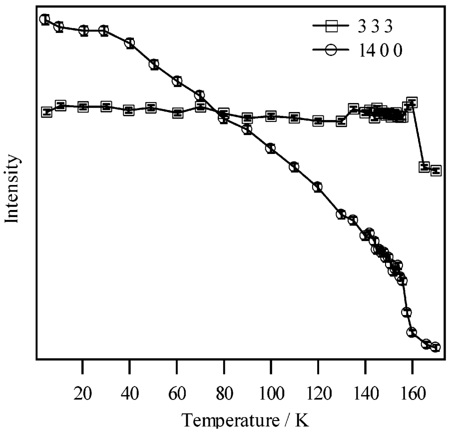

Figure 2. Plot of the 14 0 0 and 3 3 3 reflections of CsMnSD as a function of temperature. The data were collected as the sample was cooled from 170 to 5 K.

sions based on analysis of the centroids of the 1034 strongest reflections at 5 K were $a = 12.3680(10)$ Å, $b = 12.4803(10)$ Å, and $c = 12.3117(8)$ Å (*Pbca*). Data collection and analysis parameters are given in Table 2, and selected interatomic distances and interbond angles are listed in Table 3. The final fractional coordinates and thermal parameters are included as Supporting Information.

20 K Structural Determination of CsTiSD. The data collection and analysis parameters for the high-temperature cubic structure of CsTiSD are summarized in Table 2. The weighted least-squares refinement gave a final R factor of 0.033, a weighted R factor of 0.025, and χ^2 of 2.79 for the 1311 observables with a total of 73 variables comprising 23 positional parameters, two isotropic thermal parameters for Cs and Mn, 46 anisotropic thermal parameters for the remaining atoms, a scaling parameter, and a single parameter to describe the crystalline mosaic spread in the Becker−Coppens model for extinction. Selected interatomic distances and interbond angles are listed in Table 3; the fractional cell coordinates and thermal parameters are included as Supporting Information.

Phase Transition of CsTiSD. The discontinuous increase in intensity of the 4 0 0 and 3 3 −3 reflections of CsTiSD obtained on cooling to 12.2 K (Figure 3), with the cusp-like features evident for the strongest reflections, is indicative of a first-order transition with the release of extinction. No obvious broadening or splitting of the reflections was apparent. The intensity changes are reversible and show no signs of hysteresis.

2 K Structural Determination of CsTiSD. While the distortions of the cubic diffraction pattern for the low-temperature phase of CsTiSD are much less pronounced than those apparent for the low-temperature phase of CsMnSD, a satisfactory refinement of the data to the *Pbca* space group was obtained. The data analysis and structure refinement values are summarized in Table 2. Least-squares matching of the observed and calculated centroids of the 1697 strongest reflections at 5 K gave $a = 12.4096(8)$ Å, $b = 12.4030(8)$ Å, and $c = 12.3891(8)$ Å in space group *Pbca*, a considerably smaller spread than observed for CsMnSD. The observed spread of the three cell dimensions is also smaller than that found in a neutron powder experiment on CsTiSD at 1.44 K on HRPD at ISIS [12.42636(2), 12.39479(2), 12.38068(2) Å],[36] but this is due to the averaging over domains in each observation in the single-crystal experiment. However, the ratio of the differences between pairs in ascending order is nearly the same in the two experiments, which allows us to use with confidence the cell dimensions from the powder experiment in the single-crystal structural refinement and calculation of bond lengths and angles. Most reflections of the type $-h$ $+k$ $+l$ to 0.80 Å^{-1} in sin θ/λ and some equivalents were scanned at 2 K. The data were matched against the same model that allowed for three domains as for CsMnSD at 5 K (eq 1). In the final refinement the domain populations refined to 0.502(7):0.342(9):0.156(6). The final fractional coordinates and thermal parameters are included as Supporting Information. Selected interatomic distances and interbond angles are listed in Table 3.

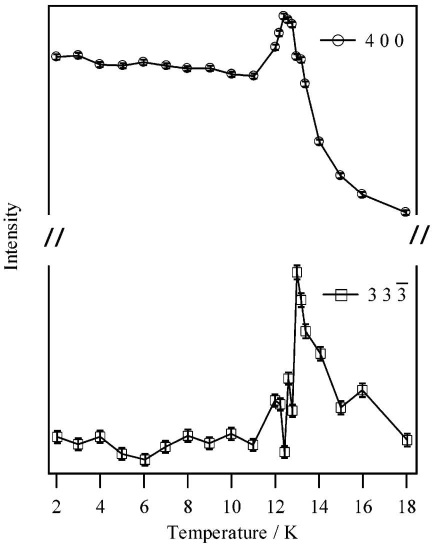

Figure 3. Plot of the 4 0 0 and 33$\bar{3}$ reflections of CsTiSD as a function of temperature. The data were collected as the sample was cooled from 20 to 2 K.

3.1.2. SXD Structure Determinations of CsTiSD, CsVSD, and CsGaSD. The merged neutron structure factor sets were used for structural refinement within GSAS.[37] For CsTiSD and CsGaSD all atoms, including the deuterium atoms, were refined with anisotropic temperature factors. For CsVSD, the merged neutron structure factor sets were of poorer quality than those for CsTiSD and CsGaSD, which impacts upon the precision but not the accuracy of the determined structural parameters. The thermal parameter of V (which has a small neutron scattering length) was held fixed at the value found for Ti in the refinement of CsTiSD, while those for Cs, S, O1, and O3a were refined isotropically. The data collection and analysis parameters for CsGaSD are summarized in Table 4, and the fractional cell coordinates and thermal parameters are included as Supporting Information. The interatomic distances and interbond angles are typical of the cesium β-alum structure, and a selection is

---

(37) Larsen, A. C.; von Dreele, R. B. *GSAS, General Structure Analysis System*; Report LAUR-86-748; Los Alamos National Laboratory: Los Alamos, NM, 1994.

Table 4. Data Collection and Analysis Parameters on the Laue Diffractometers

compound	$CsGa(SO_4)_2 \cdot 12D_2O$	$CsV(SO_4)_2 \cdot 12D_2O$
diffractometer	SXD neutron time-of-flight Laue diffractometer	LADI neutron time-of-flight Laue diffractometer on a thermal beam
detectors	64 × 64 element, 3 × 3 mm pixel, scintillator PSD	cylindrical image plate detector 4000 × 2000 pixels, 200 × 200 μ pixel cylinder sensitive area; 159 mm cylinder radius; ±144° in 2θ, ±144° in ν
detector position	$2\theta_c = 90°$, $L_2 = 158$ mm	
wavelength range	0.5−5.0 Å	0.8−3.5 Å
mol wt/g	635	616
cryst growth	aqueous solution	aqueous solution
cryst size	3.5 × 3.5 × 3.5 mm^3	2 × 2 × 2 mm^3
space group	$Pa\bar{3}$	$Pa\bar{3}$
T (K)	20	15
a (Å)	12.341(3)	12.411(3) (from SXD)
V (Å^3)	1903.8	1911.7
ρ_{calc} (g·cm^{-3})	2.244	2.141
no. of frames	28	4^a
obsd reflns	13383	5168
unique reflns $I > 3\sigma(I)$	972	1032
R_{int}	0.059	
abs coeff (cm^{-1})	$0.00 + 0.07\lambda$	
refinement program	GSAS, on F^2, $1/\sigma^2(F^2)$ weights	SFLSQ on F, $1/\sigma^2(F)$ weights
refined params	72	72
$R(F)$	0.068	0.102
$R_w(F^2)$	0.109	0.069
S	4.71	4.14

^{a} Exposure time per frame: 45 min.

included as Supporting Information, together with details of the CsTiSD and CsVSD SXD refinements.

3.1.3. LADI Structure Determination of CsVSD. The data collection and analysis parameters are summarized in Table 4. Owing to the small neutron scattering length of V, the thermal parameter for V was constrained to be the same as that for Cs. Since only relative cell dimensions can be extracted from LADI measurements, the bond lengths pertaining to the CsVSD structure were calculated using the cell parameter determined from SXD measurements (10 K) in conjunction with the fractional coordinates obtained from LADI measurements at 15 K. The fractional coordinates, thermal parameters, and selected interatomic distances and interbond angles are included as Supporting Information. We note that the precision of the refined parameters of CsVSD is comparable to that obtained for the cubic phases of CsMnSD and CsTiSD using D9 despite the greater than 20-fold reduction in data-collection time.

4. Discussion

4.1. Structures in the Cubic Phase. The atomic positions of CsMnSD and CsTiSD, obtained at 170 and 20 K, provide no intimation of the impending phase transitions, being analogous to those of CsVSD and CsGaSD. Significant differences in the cubic phase structures of the cesium sulfate alums are to be found only in the $M^{III}-O$ bond lengths, which vary in accordance with the ionic radii, and in the values of the angle φ: Those of Ga, Cr, Mn, Fe, and Mo lie in the range −19.0° to −19.7°; the φ angle of Ti is −20.4(1)°, while the magnitude of φ is larger for the V and Ru salts: −21.3(2)° and −22.0(2)°, respectively. The differences, though small, are significant, as can been seen from Figure 4, where the quantity $\Delta\varphi$ is plotted for the Ti alum relative to Ga, Cr, Mn, V, Fe, Ti, Ru, and Mo. The tervalent cations are ordered in terms of increasing $M^{III}-O$ bond length. Thus, it may be inferred that the differences in the φ angles are not related to the ionic radii of the tervalent cations, nor solely to whether the complex is formed from a first- or second-row transition metal ion. The data provide information on the *relative* stability of the complexes towards a displacement along this coordinate, which can be related to the occupancy of the t_{2g} orbitals. For aqua ions of S_6 symmetry, intermediate between T_h ($\varphi = 0°$) and D_{3d} ($\varphi = -45°$), the AOM expression for the splitting of the one-electron orbitals has a particularly simple form:[13,14]

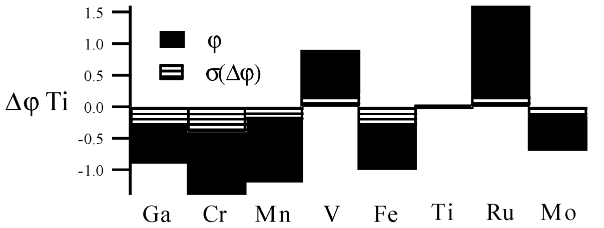

Figure 4. Bar chart showing the difference in twist angle of the titanium alum relative to all of the cesium β alums whose structures have been determined by neutron diffraction (includes the cubic phase structures of CsTiSD (20 K) and of CsMnSD (170 K)). $\Delta\varphi$ Ti denotes the quantity $\varphi(\mathrm{Ti}) - \varphi(\mathrm{M^{III}})$.

$$\Delta = 3(e_{\pi\perp} - e_{\pi\|})\sin(2\varphi) \qquad (2)$$

where $e_{\pi\perp}$ and $e_{\pi\|}$ parametrize the π-bonding normal to and in the plane of the water molecule, respectively. Spectroscopic data on the vanadium alums have been satisfactorily interpreted assuming ($e_{\pi\perp} - e_{\pi\|}$) ~ 930 cm^{-1};[38−40] this implies a splitting of the t_{2g} one-electron orbitals of the order of ~1800 cm^{-1} with the e_g orbital set lower lying. The Ti(III), V(III), and Ru(III) aqua ions alone are stabilized by a larger trigonal field, which is afforded by a greater magnitude of the twist angle, φ. The values of φ found for the Ti, V, and Ru salts can be interpreted as a compromise between the electronic preference of the aqua cations and the hydrogen-bonding constraints of the lattice. From purely electronic considerations, a greater displacement along the φ coordinate, depicted in Figure 1, would be expected for $[V(OD_2)_6]^{3+}$ relative to $[Ti(OD_2)_6]^{3+}$, as the resulting stabilization of the ^3A_g ground term of $[V(OD_2)_6]^{3+}$ is approximately twice that of the ^2E_g ground term of $[Ti(OD_2)_6]^{3+}$. Owing to the greater metal(III)−water π interaction,[14,41] a greater displacement still would be expected for the $[Ru(OD_2)_6]^{3+}$ cation.

---

(38) Tregenna-Piggott, P. L. W.; Best, S. P.; Güdel, H. U.; Weihe, H.; Wilson, C. C. *Solid State Chem.* **1999**, *145*, 460.

(39) Spichiger, D.; Carver, G.; Dobe, C.; Bendix, J.; Tregenna-Piggott, P. L. W.; Meier, R.; Zahn, G. *Chem. Phys. Lett.* **2001**, *337*, 391.

(40) Tregenna-Piggott, P. L. W.; Weihe, H.; Bendix, J.; Barra, A.-L.; Güdel, H.-U. *Inorg. Chem.* **1999**, *38*, 5928.

(41) Dolder, S.; Spichiger, D.; Tregenna-Piggott, P. L. W. *Inorg. Chem.* **2003**, *42*, 1343−1349.

Recent ab initio SCF[42] and DFT[43] calculations on gas-phase aqua ions suggest that the energy minimum of $[Ru(OD_2)_6]^{3+}$ is firmly localized in the all-horizontal D_{3d} geometry ($\varphi = -45°$). For the $[Ti(OD_2)_6]^{3+}$ and $[V(OD_2)_6]^{3+}$ cations, however, the increase in the magnitude of repulsion terms, upon increasing magnitude of φ, are predicted to outweigh the gain from increased electronic stabilization. The T_h ($\varphi = 0°$) − S_6 ($0° < \varphi < \pm 45°$) − D_{3d} ($\varphi = \pm 45°$) potential-energy surface calculated for the Ti(III) and V(III) hexaaqua cations is rather shallow, with minima at 13.6° (Ti(III)) and −9.4° (V(III)).[43] In the preceding paper[41] it was demonstrated that in aqueous solution the $[Ru(OH_2)_6]^{3+}$ cation adopts the all-horizontal D_{3d} geometry whereas the structure of $[V(OH_2)_6]^{3+}$ is closer to T_h, in agreement with theory. However, the relevance of these calculations to the solid state is questionable, given that the variation in the values of φ can be rationalized, quite adequately, in terms of elementary AOM calculations. The value of φ is anomalously negative for $[Ru(OD_2)_6]^{3+}$ and $[V(OD_2)_6]^{3+}$, suggesting that both these aqua ions exhibit a tendency to distort towards the all-horizontal D_{3d} structure. Indeed, it is noteworthy that the $[V(OH_2)_6]^{3+}$ cation adopts the all-horizontal D_{3d} geometry in the triflate salt.[44] The propensity of the vanadium alums to crystallize in the β-modification, rather than in the α-modification where $\varphi \sim 0°$,[12] may also be adduced.[16,38,45] This may suggest that the repulsion terms are not well modeled in strongly hydrogen-bonded situations.

4.2. Low-Temperature Structures of CsMnSD and CsTiSD. The structural instability exhibited by CsMnSD and CsTiSD must be related to the electronic structure of the tervalent cations, rather than to the size of the constituent molecular groups, as the ionic radii of Mn(III) and Ti(III) are encompassed by those of Ga(III) and Mo(III) (Figure 4) and the structural and spectroscopic data of CsGaSH[10,19,46] and CsMoSH[18,47] provide no indication of structural instability. From Table 1, it is seen that the ligand field imposed by the disposition of the water molecules about the metal center (Figure 1) results in orbitally degenerate ground terms for the $[Ti(OH_2)_6]^{3+}$ and $[Mn(OH_2)_6]^{3+}$ cations only. These aqua ions are subject, therefore, to first-order Jahn−Teller coupling (if spin−orbit coupling is ignored) and the symmetry of the crystal is lowered below a critical temperature (13 K for CsTiSD and 156 K for CsMnSD) when the strength of the correlation between the distortions of the Jahn−Teller centers is sufficiently large compared to the thermal energy available to the system. The large difference in the transition temperatures is a direct reflection of the different magnitudes of Jahn−Teller coupling. For CsTiSD, the unpaired electron lies in the t_{2g} orbitals, which are weakly π-antibonding. Above 13 K, the thermal energy is enough to destroy the correlation between the Jahn−Teller centers and the high-symmetry structure is retained. For CsMnSD, the high-spin d^4 electron configuration of Mn(III) gives rise to an orbitally degenerate ground term, in which the unpaired electron lies in the σ-antibonding e_g (O_h) orbital set. The energies of the orbital components of the ^5E_g (S_6) ground term are therefore extremely susceptible to perturbations of the σ-bonding framework, resulting in a stronger interaction and a higher transition temperature. This phenomenon, known as the cooperative Jahn−Teller effect,[48−51] has already been recognized as the driving force for the dramatic change in the lattice constants and magnetic properties of CsTiSD below ca. 13 K.[36] However, the low-temperature structural parameters were not known at the time of that study.

The changes in the stereochemistries of the $[Ti(OH_2)_6]^{3+}$ and $[Mn(OH_2)_6]^{3+}$ cations that accompany the phase transitions reflect the preferred geometry of the aqua ions, and the packing requirements of the crystals. In order to facilitate a comparison between the low-temperature structures of CsMnSD and CsTiSD, it is expedient to quantify the displacements of the $[Ti(OH_2)_6]^{3+}$ and $[Mn(OH_2)_6]^{3+}$ cations along their respective internal coordinates. Attention is confined to the $\nu_2(MO_6)$ stretch, the $\nu_5(MO_6)$ bend, and the $\tau[M(OH_2)_6]$ twisting libration, as the energies of the one-electron 3d orbitals are particularly sensitive to displacements along these coordinates. Examples of these symmetrized displacements are shown in Figure 5.

The $\nu_1(MO_6)$ symmetric stretching vibration, and the two components of the $\nu_2(MO_6)$ asymmetric stretching vibration, transform as $Q_a{}^s \sim \Delta z^2 + \Delta x^2 + \Delta y^2$, and $Q_\theta{}^s \sim 2\Delta z^2 - \Delta x^2 - \Delta y^2$, $Q_\epsilon{}^s \sim \sqrt{}3(\Delta x^2 - \Delta y^2)$, respectively. Displacements along these coordinates may be expressed in a basis of increments in the metal−oxygen bond lengths: $\Delta Q_a{}^s = \rho_{\nu 1}(1/\sqrt{6})(\mathbf{r_1} + \mathbf{r_4} + \mathbf{r_2} + \mathbf{r_5} + \mathbf{r_3} + \mathbf{r_6})$, $\Delta Q_{e\theta}{}^s = \rho_{\nu 2}(\cos \phi_{\nu 2})(1/\sqrt{12})(2\mathbf{r_1} + 2\mathbf{r_4} - \mathbf{r_2} - \mathbf{r_5} - \mathbf{r_3} - \mathbf{r_6})$; $\Delta Q_{e\epsilon}{}^s = \rho_{\nu 2}(\sin \phi_{\nu 2})(1/2)(\mathbf{r_2} + \mathbf{r_5} - \mathbf{r_3} - \mathbf{r_6})$, where $\mathbf{r}_i$ is a unitary displacement along the M−O$_i$ bond vector. The displacement along the $Q_a{}^s$ coordinate is given by the parameter $\rho_{\nu 1}$, which

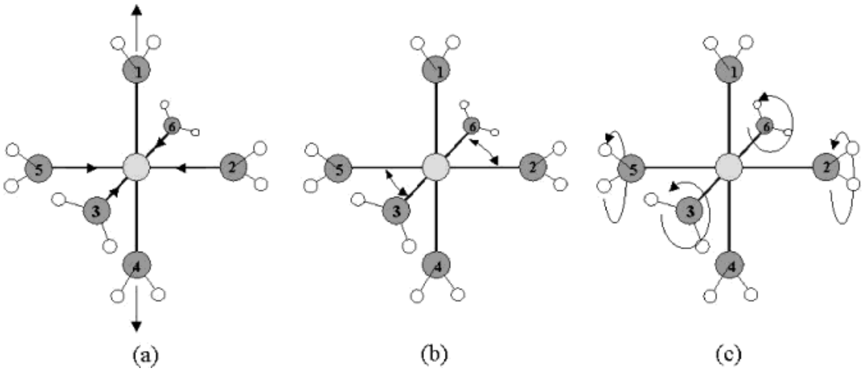

Figure 5. Examples of symmetrized distortions of a hexaaqua complex: (a) the Q_θ component of the $\nu_2(MO_6)$, e_g (T_h) stretching vibration; (b) The Q_ζ component of the $\nu_5(MO_6)$, t_g (T_h) bending vibration; (c) the Q_ζ component of the $\tau[M(OH_2)_6]$, t_g (T_h) twisting libration.

may be positive or negative. The distortion of the molecule along the components of the $\nu_2(MO_6)$ vibration is described in polar coordinates, in terms of the magnitude of the displacement vector, $\rho_{\nu2}$, and the angle, $\phi_{\nu2}$, which it makes to the Q_θ displacement vector, in the two-dimensional Q_θ, Q_ϵ coordinate space. The bond length displacements, Δr_i, are then related to $\rho_{\nu1}$, $\rho_{\nu2}$, and $\phi_{\nu2}$ as follows:

$$\Delta r_1 = \Delta r_4 = \frac{\rho_{\nu2}}{\sqrt{12}}(2\cos\phi_{\nu2}) + \frac{\rho_{\nu1}}{\sqrt{6}}$$

$$\Delta r_2 = \Delta r_5 = \frac{\rho_{\nu2}}{\sqrt{12}}(-\cos\phi_{\nu2} + \sqrt{3}\sin\phi_{\nu2}) + \frac{\rho_{\nu1}}{\sqrt{6}}$$

$$\Delta r_3 = \Delta r_6 = \frac{\rho_{\nu2}}{\sqrt{12}}(-\cos\phi_{\nu2} - \sqrt{3}\sin\phi_{\nu2}) + \frac{\rho_{\nu1}}{\sqrt{6}} \quad (3)$$

Since a displacement along $\nu_1(MO_6)$ affects all M−O bond lengths equally, $\rho_{\nu2}$ may also be expressed in terms of displacements of the M−O bond lengths from the average M−O bond length, r_{av},

$$\rho_{\nu2} = \left(\sum_1^6 (r_i - r_{av})^2\right)^{1/2} \quad (4)$$

The three components of the T_g (T_h) $\nu_5(MO_6)$ bending mode are most conveniently represented in a basis of displacements of the O−M−O bond angles. Thus a displacement along the $Q_\zeta{}^b$ component of $\nu_5(MO_6)$ depicted in Figure 5b, which transforms as $Q_\zeta{}^b \sim xy$, may be written as $\Delta Q_\zeta{}^b = \rho_{\nu5}{}^\zeta(1/2)(\boldsymbol{\alpha}_{23} + \boldsymbol{\alpha}_{56} - \boldsymbol{\alpha}_{26} - \boldsymbol{\alpha}_{35})$, where $\boldsymbol{\alpha}_{ij}$ denotes a unitary increment in the O_i−M−O_j bond angle. Correspondingly, $\Delta Q_\eta{}^b$ and $\Delta Q_\xi{}^b$ are given by $\Delta Q_\eta{}^b \sim xz = \rho_{\nu5}{}^\eta(1/2)(\boldsymbol{\alpha}_{12} + \boldsymbol{\alpha}_{45} - \boldsymbol{\alpha}_{24} - \boldsymbol{\alpha}_{15})$, $\boldsymbol{\Delta Q_\xi{}^b} \sim yz = \boldsymbol{\rho_{\nu5}{}^\xi}(1/2)(\boldsymbol{\alpha}_{13} + \boldsymbol{\alpha}_{46} - \boldsymbol{\alpha}_{16} - \boldsymbol{\alpha}_{34})$. As we are considering trigonal systems, it is convenient to construct a new set of angular displacement coordinates, $\Delta Q_z{}^b$, $\Delta Q_x{}^b$, $\Delta Q_y{}^b$, which are related to $\Delta Q_\xi{}^b$, $\Delta Q_\eta{}^b$, $\Delta Q_\zeta{}^b$ by the following transformation matrix:

$$\begin{bmatrix}\Delta Q_z{}^b \\ \Delta Q_x{}^b \\ \Delta Q_y{}^b\end{bmatrix} = \begin{bmatrix}1/\sqrt{3} & 1/\sqrt{3} & 1/\sqrt{3} \\ \sqrt{2}\sqrt{3} & -1/\sqrt{6} & -1/\sqrt{6} \\ 0 & 1/\sqrt{2} & -1/\sqrt{2}\end{bmatrix}\begin{bmatrix}\Delta Q_\zeta{}^b \\ \Delta Q_\eta{}^b \\ \Delta Q_\xi{}^b\end{bmatrix} \quad (5)$$

$Q_z{}^b$ then transforms like the axial vector $\sim z^2$ and $Q_x{}^b$, $Q_y{}^b$ together form a basis for the e_g irreducible representation in the S_6 point group. A displacement along linear combinations of the e_g (S_6) components of the $\nu_5(MO_6)$ vibration can also be represented in polar coordinates, as for the $\nu_2(MO_6)$ vibration. By analogy with eq 1, the O−M−O angular displacements, $\Delta\alpha_{ij}$, are then related to $\rho_{\nu5}{}^a$, $\rho_{\nu5}{}^e$, and $\phi_{\nu5}$ as follows:

$$\Delta\alpha_{23} = \Delta\alpha_{56} = -\Delta\alpha_{26} = -\Delta\alpha_{35} = \frac{\rho_{\nu5}{}^e}{\sqrt{24}}(2\cos\phi_{\nu5}) + \frac{\rho_{\nu5}{}^a}{\sqrt{12}}$$

$$\Delta\alpha_{12} = \Delta\alpha_{45} = -\Delta\alpha_{24} = -\Delta\alpha_{15} = \frac{\rho_{\nu5}{}^e}{\sqrt{24}}(-\cos\phi_{\nu5} + \sqrt{3}\sin\phi_{\nu5}) + \frac{\rho_{\nu5}{}^a}{\sqrt{12}}$$

$$\Delta\alpha_{13} = \Delta\alpha_{46} = -\Delta\alpha_{16} = -\Delta\alpha_{34} = \frac{\rho_{\nu5}{}^e}{\sqrt{24}}(-\cos\phi_{\nu5} - \sqrt{3}\sin\phi_{\nu5}) + \frac{\rho_{\nu5}{}^a}{\sqrt{12}} \quad (6)$$

By analogy with eq 4, the radial extent of the distortion, $\rho_{\nu5}{}^e$, is given by

$$\rho_{\nu5}{}^e = \left(\sum_1^{12} (\alpha_{ij} - \alpha_{av})^2\right)^{1/2} \quad (7)$$

A displacement along the $Q_z{}^b$ component of $\nu_5(MO_6)$ can also be represented in terms of the polar coordinates of the oxygen atoms relative to the 3-fold axis: $\Delta Q_z{}^b = \rho_{\nu5}{}^a(1/\sqrt{6})(\boldsymbol{\theta}_1 + \boldsymbol{\theta}_2 + \boldsymbol{\theta}_3 - \boldsymbol{\theta}_4 - \boldsymbol{\theta}_5 - \boldsymbol{\theta}_6)$.

The symmetric twisting librations, $\tau[M(OH_2)_6]$, transform as T_g in the T_h point group and may be represented in a basis of displacements along the twisting coordinates of the six water molecules. Thus, a displacement along the $Q_\zeta{}^\tau$ libration, depicted in Figure 5c, may be written as $\Delta Q_\zeta{}^\tau = \rho_\tau{}^\zeta$-$(1/2)(\boldsymbol{\varphi}_2 - \boldsymbol{\varphi}_5 + \boldsymbol{\varphi}_3 - \boldsymbol{\varphi}_6)$. Analogous expressions follow for $\Delta Q_\xi{}^\tau$ and $\Delta Q_\eta{}^\tau$. Just as for the $\nu_5(MO_6)$ vibration, displacement coordinates, $\Delta Q_z{}^\tau$, $\Delta Q_x{}^\tau$, $\Delta Q_y{}^\tau$, which transform as a_g, and components of e_g in the S_6 point group, can be constructed by applying the transformation matrix, in eq 5. Displacements along the twisting coordinates of the six water molecules are then related to $\rho_\tau{}^a$, $\rho_\tau{}^e$, and ϕ_τ as follows:

$$\Delta\varphi_1 = -\Delta\varphi_4 = \frac{\rho_\tau{}^e}{\sqrt{12}}(2\cos\phi_\tau) + \frac{\rho_\tau{}^a}{\sqrt{6}}$$

$$\Delta\varphi_2 = -\Delta\varphi_5 = \frac{\rho_\tau{}^e}{\sqrt{12}}(-\cos\phi_\tau + \sqrt{3}\sin\phi_\tau) + \frac{\rho_\tau{}^a}{\sqrt{6}}$$

$$\Delta\varphi_3 = -\Delta\varphi_6 = \frac{\rho_\tau{}^e}{\sqrt{12}}(-\cos\phi_\tau - \sqrt{3}\sin\phi_\tau) + \frac{\rho_\tau{}^a}{\sqrt{6}} \quad (8)$$

$$\rho_\tau = \left(\sum_1^6 (\varphi_i - \varphi_{av})^2\right)^{1/2} \quad (9)$$

The water molecules coordinated to the Ti and Mn centers in the low-symmetry structures are labeled d, e, and f in Table 3. We now have to decide which are 1, 2, and 3 in eqs 3, 6,

---

(42) Åkesson, R.; Pettersson, L. G. M.; Sandström, M.; Wahlgren, U. *J. Am. Chem. Soc.* **1994**, *116*, 8691.

(43) Kallies, B.; Meier, R. *Inorg. Chem.* **2001**, *40*, 3101.

(44) Cotton, F. A.; Fair, C. K.; Lewis, G. E.; Mott, G.; Moss, F. K.; Schultz, A. J.; Williams, M. J. *J. Am. Chem. Soc.* **1984**, *106*, 5319.

(45) Beattie, J. K.; Best, S. P.; Del Favero, P.; Skelton, B. W.; Sobolev, A. N.; White, A. H. *J. Chem. Soc., Dalton Trans.* **1996**, 1481.

(46) Tregenna-Piggott, P. L. W.; Güdel, H.-U. *Inorg. Chem.* **2001**, *40*, 5497.

(47) Armstrong, R. S.; Beattie, J. K.; Best, S. P.; Cole, B. D.; Tregenna-Piggott, P. L. W. *J. Raman Spectrosc.* **1995**, *26*, 921.

(48) Englman, R. *The Jahn-Teller Effect in Molecules and Crystals*; Wiley: London, 1972.

(49) Gehring, G. A.; Gehring, K. A. Co-operative Jahn-Teller Effects. *Rep. Prog. Phys.* **1975**, *38*, 1.

(50) Bersuker, I. B. *The Jahn-Teller Effect and Vibronic Interactions in Modern Chemistry:* Plenum Press: New York, 1984.

(51) Kaplan, M. D.; Vekhter, B. G. *Co-operative Phenomena in Jahn-Teller Crystals*; Plenum Press: New York, 1995.

Table 5. Displacements along the Stretching, Bending, and Twisting Coordinates of the $[Ti(OD_2)_6]^{3+}$ and $[Mn(OD_2)_6]^{3+}$ Cations, Resulting from the Cubic to Orthorhombic Phase Transitions[a]

displacement coordinate		Ti	Mn
stretch	$\rho_{\nu 1}$/Å	−0.002(3)	0.014(2)
	$\rho_{\nu 2}$/Å	0.013(3)	0.234(2)
	$\phi_{\nu 2}$/deg	267(8)	1.2(4)
bend	$\rho_{\nu 5}{}^{a}$/deg	−0.03(15)	−0.09(15)
	$\rho_{\nu 5}{}^{e}$/deg	2.65(15)	0.89(15)
	$\phi_{\nu 5}$/deg	72(3)	142(15)
twist	$\rho_{\tau}{}^{a}$/deg	0.0(4)	0.0(3)
	$\rho_{\tau}{}^{e}$/deg	2.6(4)	1.0(3)
	ϕ_{τ}/deg	184(5)	120(30)

[a] The relationship between the tabulated quantities and the internal coordinates of the aqua ions is given through eqs 3, 6, and 8.

and 8; the designation is arbitrary. For both hexaaqua cations, the metal−oxygen bonds are closely aligned with the crystallographic axes (see Supporting Information). A labeling scheme is chosen such that the metal−water(1) bond vector lies along the longest unit cell axis, and the metal−water(3) bond vector lies along the shortest. For the $[Mn(OH_2)_6]^{3+}$ cation, this is achieved by the following substitution: water(e) = water(1), water(d) = water(2), and water(f) = water(3); whereas for the $[Ti(OH_2)_6]^{3+}$ cation, water(d) = water(1), water(e) = water(2), and water(f) = water(3). For example, $\phi_{\nu 2} = 1.2(4)°$ for $[Mn(OH_2)_6]^{3+}$, but 267(8)° for $[Ti(OH_2)_6]^{3+}$. This tells one that the longest metal−oxygen bond lies along the longest unit cell axis for $[Mn(OH_2)_6]^{3+}$, but along the shortest for $[Ti(OH_2)_6]^{3+}$. Equations 3, 6, and 8 were solved numerically using the Mathematica program, and the results are listed in Table 5.

We begin by discussing the structural chemistry of CsMnSD at 170 and 5 K, with reference to Table 3, and Figure 6, which shows a fragment of the unit cell in the high- and low-symmetry phases. At 170 K, all Mn−O bond lengths are equal and the O−M−O bond angles are close to 90°. The major manifestation of the phase transition is a pronounced tetragonal elongation of the MnO_6 framework ($\rho_{\nu 2} = 0.234(2)$ Å). The degree of rhombicity in the Mn−O bond lengths is small but significant (Mn−O(d) = 1.929(1) Å, Mn−O(f) = 1.924(1) Å, $\phi_{\nu 2} = 1.2(4)°$) There is also a slight displacement along the totally symmetric breathing mode, resulting in an increase in the average Mn−O bond length ($\rho_{\nu 1} = 0.014(2)$ Å). The MnO_6 framework remains closely aligned with the crystallographic axes, and the relative magnitudes of the Mn−O bond lengths coincide with those of the cell parameters. The O−Mn−O bond angles at 5 K are within 0.3° of their values at 170 K. Nevertheless, the distortion along the e_g component of the $\nu_5(MO_6)$ bending mode is significant ($\rho_{\nu 5}{}^{e} = 0.89(15)°$, $\phi_{\nu 5} = 142(15)°$).

The distortion of the MnO_6 framework is accompanied by pronounced changes in the Mn−O−H···O hydrogen bond lengths. The Mn−O(d) and Mn−O(f) bonds contract upon cooling, with the result that the O(d) and O(f) oxygen atoms become more electropositive. Hence, the O(d)−H···O and O(f)−H···O hydrogen bond lengths decrease, and the respective O−H bond lengths increase. Conversely, the increase in the Mn−O(e) bond length gives rise to a weaker O(e)−H···O hydrogen bond. The four $[Mn(OH_2)_6]^{3+}$ cations in the unit cell are connected by a complex hydrogen-bonding network via the $[SO_4]^{2-}$ and $[Cs(OH_2)_6]^{+}$ units. The phase transition does not result in any significant changes in the bond lengths and angles of the sulfate anion; its geometry remains close to a perfect tetrahedron. However, in order to accommodate the bond-length changes, the sulfate anions are displaced relative to the $[Mn(OH_2)_6]^{3+}$ cations in the unit cell, and are rotated with respect to the crystallographic axes. The Cs atoms are similarly displaced, but their distance relative to the S atom remains constant. The $[Cs(OH_2)_6]^{+}$ unit is significantly distorted, this being the softest part of the lattice.

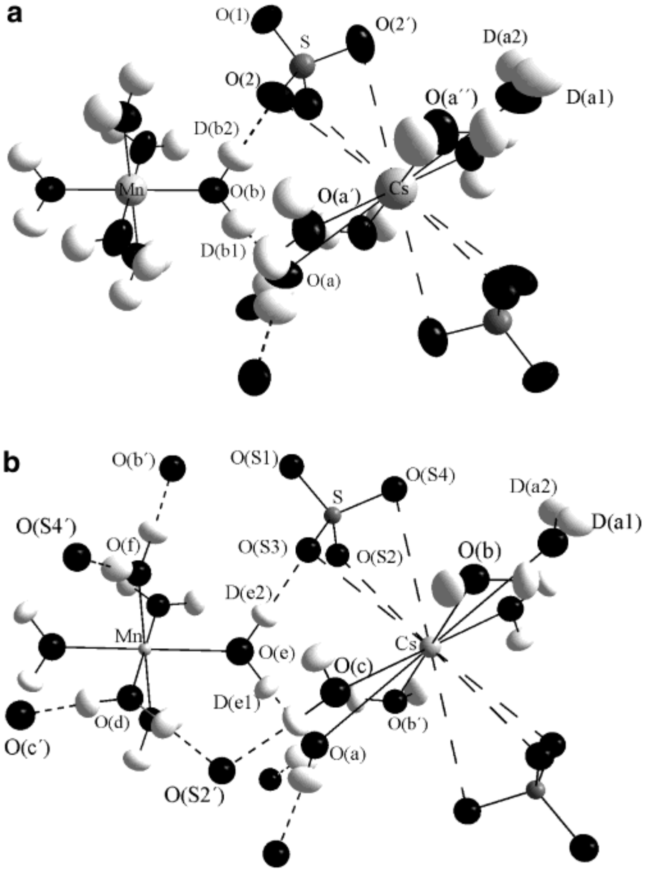

Figure 6. Molecular units which comprise the CsMnSD structure at 170 K (a) and 5 K (b). In each case, the positions of the atoms labeled Mn and Cs are related by the symmetry operation 0, 0.5, 0; the positions of the atoms labeled Mn and S by the symmetry operation $-0.5 + x, y, 0.5 - z$; and the positions of the atoms labeled Cs and S by the symmetry operation $1 - x, 1 - y, 1 - z$. Atoms are drawn at the 90% probability level.

The low-temperature structure of CsTiSD contrasts greatly with that of CsMnSD. The change in the Ti−O bond lengths is only just significant, $\rho_{\nu 2} = 0.013(3)$ Å, and the longest Ti−O bond is now directed along the *c* axis ($\phi_{\nu 2} = 267(8)°$), the smallest orthorhombic cell parameter. The structural changes that occur are all smaller than those documented for CsMnSD, except in two respects. Changes in both the O−Ti−O bond angles and the disposition of the water molecules about the tervalent cation are significantly larger ($\rho_{\nu 5}{}^{e} = 2.65(15)°$, $\rho_{\tau}{}^{e} = 2.7(4)°$). The angular displacements are accommodated by a realignment of the $[SO_4]^{2-}$ and $[Cs(OH_2)_6]^{+}$ groups. The concomitant change in the stereochemistry of the $[Ti(OH_2)_6]^{3+}$ cations and a displacement of the sulfate anions are in accordance with expectations based on the variable-temperature Raman spectrum, which shows a pronounced softening of a low-wavenumber phonon, assigned to a lattice mode of the sulfate anion, coupled to the internal modes of the $[Ti(OH)_6]^{3+}$ cation.[36] Coupling between lattice modes of this type and the orbitally degenerate electronic states, localized on the Ti(III) and Mn(III) cations, is needed to enable the transmission of long-range order.[49,51] The magnetic properties of the $[Ti(OH_2)_6]^{3+}$ cation in the β-alums are largely governed by coupling to this lattice mode, more by virtue of its low energy than by the magnitude of the coupling coefficient.[52]

4.3. Calculations of the Stability of the Ti(III) and Mn(III) Aqua Ions as a Function of Displacements along the $\nu_2(MO_6)$, $\nu_5(MO_6)$, and $\tau[M(OH_2)_6]$ Coordinates. In section 4.1 it was demonstrated that the values of φ found for the hexaaqua cations could be rationalized as a compromise between the electronic preference of the aqua ions and the hydrogen-bonding constraints of the crystal. Of great interest is the extent to which this compromise governs the low-temperature structures of the $[Mn(OH_2)_6]^{3+}$ and $[Ti(OH_2)_6]^{3+}$ ions. The low-temperature structural data identify displacements along the $\nu_2(MO_6)$, $\nu_5(MO_6)$, and $\tau[M(OH_2)_6]$ vibrational coordinates. Do all these distortions arise as a consequence of the electronic preference of the aqua ions? To what extent are they dictated by the packing constraints of the crystal? To address these questions we examine how the energy of the molecule varies as a function of displacements along these coordinates. For high-symmetry molecules, group theory can be utilized to identify the optimum value of ϕ, as the energy minimum corresponds to the cokernel subgroup, in accordance with the epikernel principle.[53] For example, the $T\otimes e$ and $E\otimes e$ Jahn–Teller interactions result in three energy minima, which are related by 120° and 240° rotations about the energy axis. For a molecule with exact O_h symmetry, the kernel group is D_{2h} but the cokernel group is D_{4h}. In the case of the commonly considered $E\otimes e_{\nu 2}$ Jahn–Teller problem, the points of minimum energy correspond to tetragonal elongations/compressions of the ML_6 framework. This work concerns structural anomalies arising from complexes on crystal sites of S_6 symmetry, where there is no cokernel group. All molecular geometries in the $E\otimes e$ subspace correspond to the kernel group, which is C_i, and the geometry of lowest energy must be determined numerically.

The principal theoretical method we have employed in this endeavor is the angular overlap model (AOM), which has proved to be very successful in predicting the sign and magnitude of the trigonal field for various geometries of the $[V(OH_2)_6]^{3+}$ cation.[13,38-40] For an appropriate set of parameters, therefore, it is anticipated that the AOM will also provide a reasonable estimate of the ground-state energy along components of $\nu_5(MO_6)$ and $\tau[M(OH_2)_6]$, as displacements along these coordinates are treated rigorously within the model.[54] For displacements along the $\nu_2(MO_6)$ mode, the magnitude of the bonding parameters e_σ and e_π were assumed to exhibit a $1/r^5$ and $1/r^6$ dependence on the bond length, respectively. AOM calculations were performed using the program LIGFIELD.[55] Unless otherwise stated, the AOM bonding parameters employed are the same as those previously determined for the $[V(OH_2)_6]^{3+}$ cation in RbVSH,[38] which is isostructural with CsVSH, namely, $e_\sigma = 6950$ cm^{-1}, $e_{\pi\perp} = 930$ cm^{-1}, and $e_{\pi\parallel} = 0$ cm^{-1}. These parameters correspond to a value of the octahedral ligand field splitting parameter, Δ_o, of 19350 cm^{-1}, which is in good agreement with the energy of the $^2T_{2g} \rightarrow {}^2E_g$ (O_h) transition of $[Ti(OH_2)_6]^{3+}$. For octahedrally coordinated Mn(III) complexes, the AOM predicts a tetragonally compressed geometry to be favored over the tetragonally elongated geometry, which is invariably found experimentally, a discrepancy attributable to the neglect of higher-order effects.[56] For the examination of the stability of the $[Mn(OH_2)_6]^{3+}$ complex as a function of changes in the Mn–O bond lengths, one has recourse to the density functional theory (DFT) method, which has proved useful in calculating quantities relating to Jahn–Teller problems.[57,58] It should be emphasized that whereas the AOM method yields the relative energies of the electronic states in a given geometry, the DFT method yields the total energy of the complex. That we have ever entertained a degree of skepticism concerning the relevance of gas-phase ab initio calculations of aqua ions to the solid state is evinced by the conclusions made in section 4.1. No account is taken of hydrogen bonding, which is an integral component of metal–water bonding in crystalline hydrates. The results of the DFT calculations are deemed to be of value only when a series of calculations along a given coordinate betokens a clear trend, or when the results may be complemented by AOM calculations. All single-point energy calculations were carried out with the Gaussian 98 package (release A.9)[59] for charge-neutral models of $[Mn(H_2O)_6]^{3+}$ and $[Ti(H_2O)_6]^{3+}$ in the $M_s = 2$ and $^1/_2$ microstates, respectively, and converged to tight solutions. For this purpose we adopted the commonly used spin-unrestricted B3LYP functional and the basis set 6–311G provided by the Gaussian 98 package.

---

(52) Tregenna-Piggott, P. L. W.; O'Brien, M. C. M.; Pilbrow, J. R.; Güdel, H.-U.; Best, S. P.; Noble, C. *J. Chem. Phys.* **1997**, *107*, 8275.

(53) Ceulemans, A.; Beyens, D.; Vanquickenborne, L. G. *J. Am. Chem. Soc.* **1984**, *106*, 5824.

(54) Schäffer, C. E. *Struct. Bonding* **1968**, *5*, 68–95.

(55) Bendix, J. *LIGFIELD*, ver. 0.92; Department of Chemistry, University of Copenhagen: Copenhagen, Denmark, 1998.

(56) Bacci, M. *Chem. Phys. Lett.* **1978**, *58*, 537. Bacci, M. *Chem. Phys.* **1979**, *40*, 237–244.

(57) Bruyndonckx, R.; Daul, C.; Manoharan, P. T.; Deiss, E. *Inorg. Chem.* **1997**, *36*, 4251.

(58) Kundu, T. K.; Bruyndonckx, R.; Daul, C.; Manoharan, P. T. *Inorg. Chem.* **1999**, *38*, 3931.

(59) Frisch, M. J.; Trucks, G. W.; Schlegel, H. B.; Scuseria, G. E.; Robb, M. A.; Cheeseman, J. R.; Zakrzewski, V. G.; Montgomery, J. A., Jr.; Stratmann, R. E.; Burant, J. C.; Dapprich, S.; Millam, J. M.; Daniels, A. D.; Kudin, K. N.; Strain, M. C.; Farkas, O.; Tomasi, J.; Barone, V.; Cossi, M.; Cammi, R.; Mennucci, B.; Pomelli, C.; Adamo, C.; Clifford, S.; Ochterski, J.; Petersson, G. A.; Ayala, P. Y.; Cui, Q.; Morokuma, K.; Malick, D. K.; Rabuck, A. D.; Raghavachari, K.; Foresman, J. B.; Cioslowski, J.; Ortiz, J. V.; Stefanov, B. B.; Liu, G.; Liashenko, A.; Piskorz, P.; Komaromi, I.; Gomperts, R.; Martin, R. L.; Fox, D. J.; Keith, T.; Al-Laham, M. A.; Peng, C. Y.; Nanayakkara, A.; Gonzalez, C.; Challacombe, M.; Gill, P. M. W.; Johnson, B. G.; Chen, W.; Wong, M. W.; Andres, J. L.; Head-Gordon, M.; Replogle, E. S.; Pople, J. A. *Gaussian 98*, Gaussian, Inc.: Pittsburgh, PA, 1998.

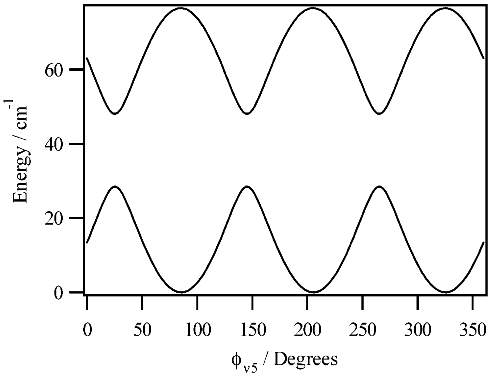

Figure 7. AOM calculation of the energy of the ^2E_g (S_6) ground term of titanium(III) as a function of $\phi_{\nu5}$, with $\rho_{\nu5}$ set to the experimental value of 2.65° (the experimentally determined value). All other internal coordinates were fixed at the values calculated from the 20 K structural data.

Analysis of the Low-Temperature Structure of the $[Ti(OH_2)_6]^{3+}$ Complex. Inspection of Table 5 reveals that the $[Ti(OH_2)_6]^{3+}$ complex is displaced significantly along all three of the asymmetric vibrations under consideration. The splitting of the ^2E_g ground term, calculated using the AOM, for the experimentally determined displacements along $\nu_2(MO_6)$, $\nu_5(MO_6)$, and $\tau[M(OH_2)_6]$, considered separately, are 28, 72, and 96 cm^{-1}, respectively. The relative magnitudes of these quantities broadly reflect the degree of Jahn−Teller coupling between the ^2E_g ground term and each of the three modes in question. Whereas the orbitally degenerate ground term of Mn(III) is strongly coupled to the $\nu_2(MO_6)$ mode, the $\nu_5(MO_6)$ and $\tau[M(OH_2)_6]$ modes dominate the Jahn−Teller coupling interaction of $[Ti(OH_2)_6]^{3+}$. The multimode nature of the Jahn−Teller coupling interaction in CsTiSD is also borne out by the isotopic dependence of the EPR spectrum, which provides a poignant illustration of the importance of coupling of the ^2E_g ground term with the $\tau[M(OH_2)_6]$ mode.[52]

Let us now consider how the energies of the t_{2g} one-electron orbitals vary as a function of ϕ, beginning with $\phi_{\nu5}$, with $\rho_{\nu5}^{e}$ fixed at the experimentally determined value of 2.65(15)°. AOM calculations were performed for different geometries of $[Ti(OH_2)_6]^{3+}$, with the twist angle, φ, varied between 0° and −45°. The equilibrium O−Ti−O bond angles were set to those derived from the 20 K neutron structure of CsTiSD. With φ set to −45°, the complex possesses all-horizontal D_{3d} symmetry, with cokernel C_{2h} geometries in the e_g displacement plane at $\phi_{\nu5} = 0°, 120°$, and 240°. The calculated energy minima occur at these geometries, in accordance with the epikernel principle. With $\varphi = 0°$, the point symmetry of the molecule would be T_h if not for the very slight trigonal elongation of the TiO_6 framework. The energy minima now occur at $\phi_{\nu5} = 60°, 180°$, and 300°. Results from the calculation with $\varphi = -21.3°$, the value obtained from the 20 K structure of CsTiSD, are shown graphically in Figure 7. The figure is confined to the variation of the energies of the states of the ^2E_g ground term of Ti(III), as a function of the displacement angle $\phi_{\nu5}$. The minima now occur at 86°, 206°, and 326°. A displacement along Q_z^{b} gives rise to a moderate change in the magnitude of the trigonal field. For a displacement along Q_z^{b} of $\rho_{\nu5}^{a} = -1°$, the energy of the e_g orbital set is lowered by 40 cm^{-1}. There is, however, no further displacement of the $[Ti(OH_2)_6]^{3+}$ complex along this coordinate upon cooling from 20 to 2 K. Analogous AOM calculations were performed as a function of $\phi_{\nu2}$ and ϕ_{τ} with $\rho_{\nu2}$ and ρ_{τ}^{e} set to the experimental values of 0.013 Å and 2.6°, respectively. For both coordinates, the barrier height between the three equivalent minima was calculated to be exceedingly small.

We now address the question of whether for the experimental values of $\rho_{\nu2}$, $\rho_{\nu5}^{e}$, and ρ_{τ}^{e} the corresponding values of $\phi_{\nu2}$, $\phi_{\nu5}$, and ϕ_{τ} reflect the electronic preference of the $[Ti(OH_2)_6]^{3+}$ cation. A rigorous approach to calculating the energy minimum would involve the calculation of an inordinate number of points over the six-dimensional potential energy surface; a task of which the labor would not be repaid by the advantage. Instead we put this question: given the experimental values of ϕ for two of the distortion coordinates, what is the value of ϕ for the third which maximizes the stabilization of the ground state? One of the angles ϕ is varied at a time, while the others are held fixed at the experimentally determined values. The energy of the ground state as a function of $\phi_{\nu5}$ and ϕ_{τ} was calculated using the AOM; the corresponding calculation as a function of $\phi_{\nu2}$ was calculated using both the AOM and DFT. The results are displayed graphically in Figure 8. In each case the calculated energy as a function of ϕ yields only one minimum; and the experimental value is very close to the value of ϕ of lowest energy: a beautiful result! For the given values of $\rho_{\nu2}$, $\rho_{\nu5}^{e}$, and ρ_{τ}^{e} the corresponding values of $\phi_{\nu2}$, $\phi_{\nu5}$, and ϕ_{τ} are such as to maximize the splitting of the ^2E_g ground term, which is calculated to be 227 cm^{-1}, in broad agreement with predictions based upon analysis of the magnetic properties of the $[Ti(OH_2)_6]^{3+}$ cation in this crystal system.[52,60]

Analysis of the Low-Temperature Structure of the $[Mn(OH_2)_6]^{3+}$ Complex. The change in the stereochemistry of the $[Mn(OH_2)_6]^{3+}$ complex on cooling CsMnSD through the phase transition is clearly dominated by a large displacement along the $Q_{e\theta}^{s}$ component of the $\nu_2(MO_6)$ vibration: the quintessential Jahn−Teller distortion. However, the value of $\phi_{\nu2}$ is a little greater than zero as is the distortion along the e_g component of the $\nu_5(MO_6)$ mode; the MnO_6 framework is thus distorted slightly from idealized D_{4h} symmetry. Although the degree of rhombicity is very small, the magnitude of the rhombic zero-field-splitting parameter, E, in octahedrally coordinated Mn(III) and Cr(II) complexes is very sensitive to small distortions of the ML_6 framework[61] (although for the $[Mn(OH_2)_6]^{3+}$ complex, the large value of E arises primarily from the anisotropic π-bonding interaction).[62] It is of interest, therefore, to gauge the extent to which the rhombicity results from the electronic preference of the $[Mn(OH_2)_6]^{3+}$ complex.

In Figure 9 is shown the energy of the $[Mn(OH_2)_6]^{3+}$ complex as a function of $\phi_{\nu2}$, calculated by DFT, with $\rho_{\nu1}$

---

(60) Dubicki L.; Riley, M. J. *J. Chem. Phys.* **1997**, *106*, 1669.

(61) Weihe, H. Manuscript in preparation.

(62) Basler, R.; Tregenna-Piggott, P. L. W.; Andres, H. P.; Dobe, C.; Güdel, H.-U.; Janssen, S.; McIntyre, G. J. *J. Am. Chem. Soc.* **2001**, *123*, 3377.

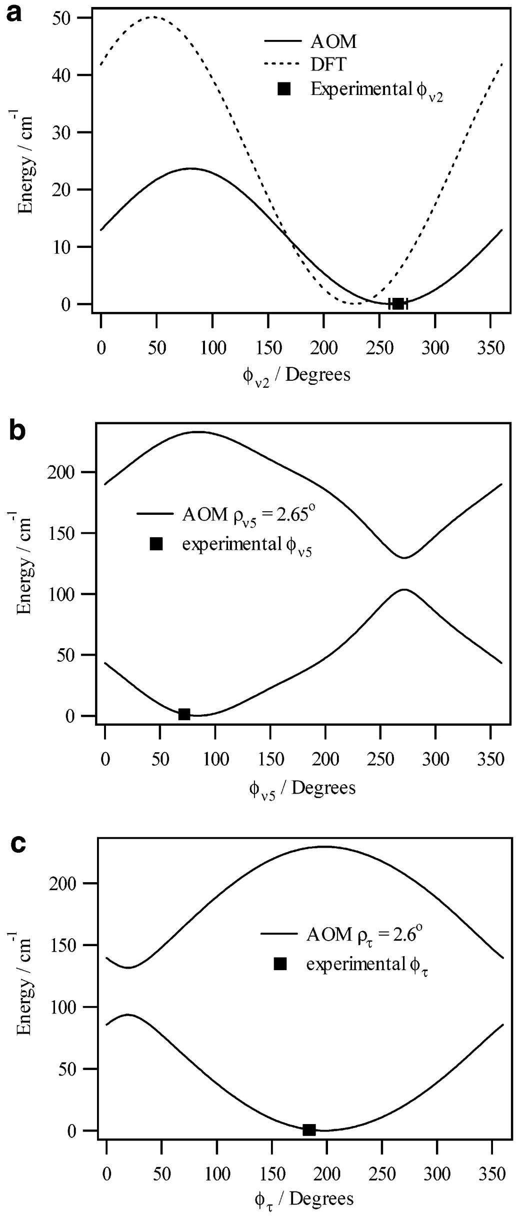

Figure 8. (a) AOM and DFT calculations of the energy of the ground state of the $[Ti(OH_2)_6]^{3+}$ cation as a function of $\phi_{\nu 2}$, with $\rho_{\nu 1}$ and $\rho_{\nu 2}$ set to -0.002 and 0.013 Å, respectively. All other internal coordinates were fixed at the values calculated from the 2 K structural data. The equilibrium Ti−O bond distance was calculated from the 20 K neutron diffraction data of CsTiSD. (b) AOM calculation of the energies of the components of the ^2E_g (S_6) ground term of the $[Ti(OH_2)_6]^{3+}$ cation as a function of $\phi_{\nu 5}$, with $\rho_{\nu 5}{}^{e}$ set to 2.65°. All other internal coordinates were fixed at the values calculated from the 2 K structural data. The equilibrium O−Ti−O bond angles were calculated from the 20 K neutron diffraction data of CsTiSD. (c) AOM calculation of the energies of the components of the ^2E_g (S_6) ground term of the $[Ti(OH_2)_6]^{3+}$ cation as a function of ϕ_{τ}, with ρ_{τ} set to 2.7°. All other internal coordinates were fixed at the values calculated from the 2 K structural data. The equilibrium φ twist angle was calculated from the 20 K neutron diffraction data of CsTiSD. For all three calculations, the spin−orbit coupling parameter was set to zero.

and $\rho_{\nu 2}$ set to the experimentally determined values of 0.014 and 0.234 Å. The other internal coordinates of the molecule are fixed at values corresponding to the 170 K geometry in Figure 9a and to the 5 K geometry in Figure 9b. In both calculations the minimum does not occur at $\phi_{\nu 2} = 0$ but at 0.90(2)° (170 K calculation) and 0.58(2)° (5 K calculation).

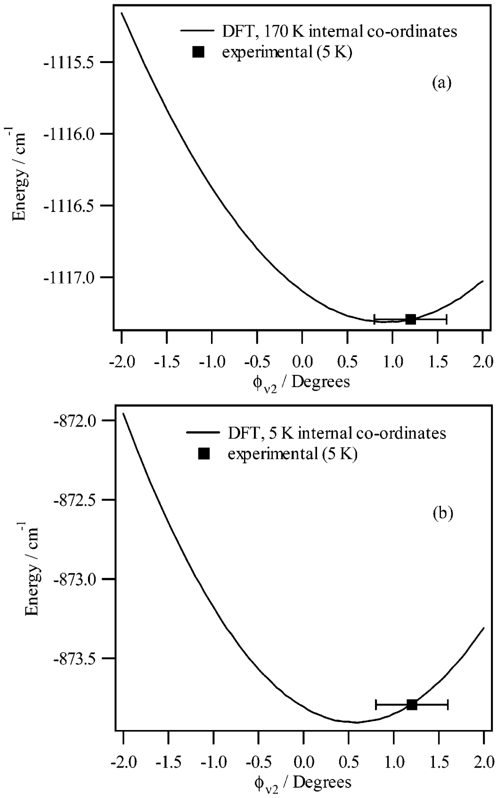

Figure 9. Ground-state energy of the $[Mn(OH_2)_6]^{3+}$ cation as a function of $\phi_{\nu 2}$, with $\rho_{\nu 1}$ and $\rho_{\nu 2}$ set to the experimentally determined values of 0.014 and 0.234 Å, respectively, calculated using the DFT method. The other internal coordinates were fixed at the values determined from the 170 K (a) and 5 K (b) structural refinements. The energies are plotted relative to the energy of the 170 K structure.

The DFT calculations suggest that the energy minima correspond to the equatorial Mn−O bonds being of slightly unequal length, i.e., with Mn−O(e) as the longest bond, the calculated energy minimum corresponds to Mn−O(d) being slightly greater than Mn−O(f); in auspicious agreement with experiment ($\phi_{\nu 2} = 1.2(4)°$). Nevertheless, given that the energy and bond length differences under consideration are very small, and our desire not to be seen embracing DFT à la carte, we must conclude that the results of these calculations are inconclusive. What they do demonstrate is that, in the absence of cokernel symmetries in the $\nu_2(ML_6)$ subspace, the minimum does not necessarily correspond to a tetragonally distorted ML_6 framework, as is usually assumed; rhombicity in the metal−ligand bond lengths should not automatically be imputed to lattice strain. The calculations presented in Figure 9 were undertaken with the O−H bond lengths constrained to the experimental values, which are larger than the optimized values for the free complex, due to hydrogen bonding. If the 170 K calculation is repeated and the O−H bond lengths are optimized for each value of $\phi_{\nu 2}$, then the minimum occurs at $-0.89(6)°$, suggesting that the strength of hydrogen bonding could influence the optimum value of $\phi_{\nu 2}$. We have also undertaken DFT calculations on the $MnCl_6^{3-}$ ion with the Cl−Mn−Cl bond angles constrained to the O−Mn−O bond angles obtained from the 170 K structural determination. In this instance we found $\phi_o = 0.00(1)°$.

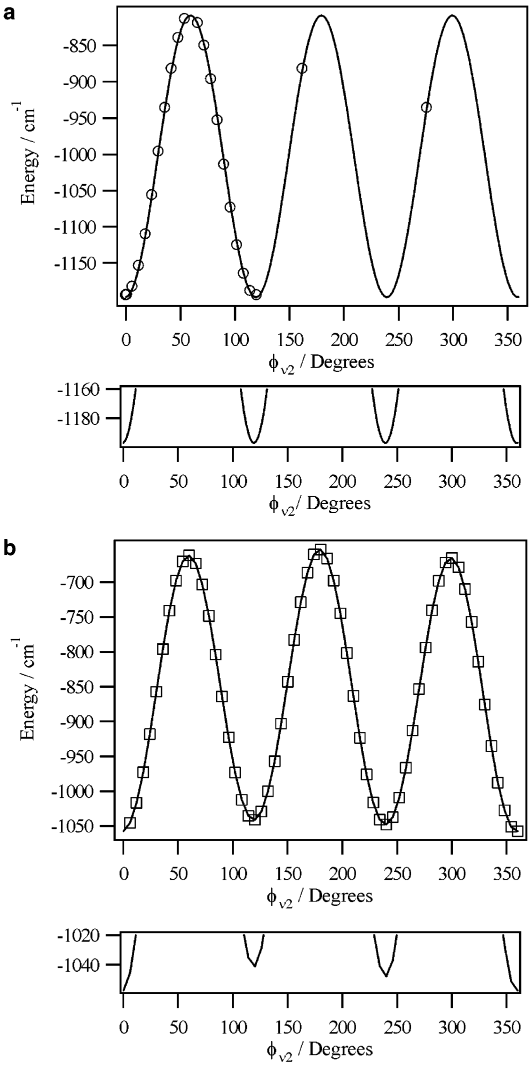

Figure 10. Energy of the $[Mn(OH_2)_6]^{3+}$ complex as a function of $\phi_{\nu 2}$, relative to the equilibrium S_6 geometry, with $\rho_{\nu 1}$ and $\rho_{\nu 2}$ set to 0.014 and 0.234 Å, respectively. The circles and squares denote the energies calculated using the DFT method, with the O−Mn−O bond angles frozen at the 170 and 5 K values, respectively. The O−H bond lengths were optimized in each calculation, including that corresponding to the equilibrium geometry. The curve through the circles in the upper figure represents the least-squares fit of the energy calculated using eq 9, to the calculated points; the parameters are given in the text. The curve through the squares in the lower figure is simply a line joining all the points.

In T_h symmetry, a displacement along any linear combination of the components of the $\nu_5(MO_6)$ bending mode does not give rise to a first-order splitting of the ^5E_g ground term of $[Mn(OH_2)_6]^{3+}$. The symmetry restriction is lifted in S_6 symmetry though the splitting is very small. In order to investigate the effect of the distortion along the $\nu_5(MO_6)$ bending mode, we have calculated the energy of the $[Mn(OH_2)_6]^{3+}$ complex as a function of $\phi_{\nu 2}$ keeping $\rho_{\nu 1}$ and $\rho_{\nu 2}$ fixed at the experimentally determined values of 0.014 and 0.234 Å, but optimizing the O−H bond lengths for each geometry; the results are displayed in Figure 10. The O−Mn−O bond angles are fixed at the values corresponding to the 170 K structure, for the calculation displayed in Figure 10a, and at the 5 K values for the calculation displayed in Figure 10b. For the 170 K calculation, the energy of the molecule is repeated in cycles of $\phi_{\nu 2} = 120°$, as the structures of the complex at $\phi_{\nu 2}$, $\phi_{\nu 2} + 120°$, and $\phi_{\nu 2} + 240°$ are related to one another by $2\pi/3$ and $4\pi/3$ rotations about the axis equating to the 3-fold axis at $\rho_{\nu 2} = 0$. Superimposed is a curve calculated with the equation

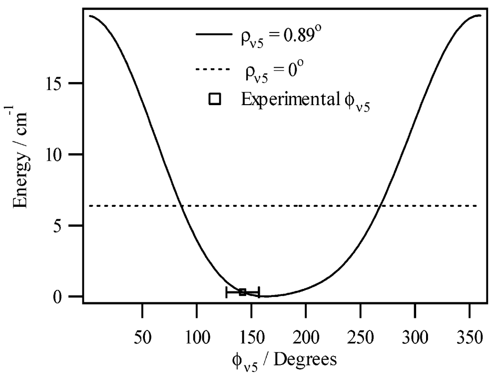

Figure 11. Energy of the ^5A_g ground term of the $[Mn(OH_2)_6]^{3+}$ cation as a function of displacements along the e_g (S_6) component of the $\nu_5(MO_6)$ vibration. The equilibrium O−Mn−O bond angles were calculated from the 170 K neutron diffraction data of CsMnSD. The angles describing displacements along the twisting librations were held constant at the values determined from the 5 K structure. The AOM bonding parameters used were chosen to mimic a tetragonal elongation of the $[Mn(OH_2)_6]^{3+}$ cation, with $\rho_{\nu 1} = 0.014$ Å, $\rho_{\nu 2} = 0.234$ Å, and $\phi_{\nu 2} = 1.2°$, and are as follows: $e_\sigma = 4934$ cm^{-1}, $e_{\pi\perp} = 617$ cm^{-1}, and $e_{\pi\|} = 0$ cm^{-1} (Mn−water(e)); $e_\sigma = 8080$ cm^{-1}, $e_{\pi\perp} = 1114$ cm^{-1}, and $e_{\pi\|} = 0$ cm^{-1} (Mn−water(d)); $e_\sigma = 8185$ cm^{-1}, $e_{\pi\perp} = 1132$ cm^{-1}, and $e_{\pi\|} = 0$ cm^{-1} (Mn−water(f)). The spin−orbit coupling parameter was set to zero and the Racah parameters B and C to 760 and 3290 cm^{-1}, respectively. The two plots displayed are for $\rho_{\nu 5} = 0°$ and 0.89° (the experimentally determined value).

$$E(\phi) = E_0 + \alpha\{1 - \cos(3(\phi - \phi_0))\} \tag{10}$$

which is commonly employed to describe the rotational potential of a one-dimensional 3-fold rotor,[63] The quantity 2α is the barrier height, and E_0 is the energy minima (relative to $\rho_{\nu 2} = 0$) which occur at $\phi = \phi_0$, $\phi_0 + 120°$, $\phi_0 + 240°$. Least-squares refinement of $E(\phi)$ to the calculated points yields $E_0 = -1191(1)$ cm^{-1}, $2\alpha = 389(1)$ cm^{-1}, $\phi_0 = -0.89(6)°$. When the distortion along the $\nu_5(MO_6)$ bending mode is included, a quite different result is obtained. Each value of $\phi_{\nu 2}$ now corresponds to a different structure, the result of which is that the 3-fold degeneracy is lifted. The energy of the structure corresponding to $\phi_{\nu 2} \sim 0°$ is lowered relative to the $\phi_{\nu 2} \sim 120°$, 240° geometries, although the energy is slightly higher in the 5 K compared to the 170 K structure calculation. We are not unduly troubled by the increase in the overall energy, as the contribution from interatomic repulsion does not take into account the environment of the aqua ion in the crystal. The results of DFT are clarified by AOM calculations, which suggest that, as a result of the small displacement along the $\nu_5(MO_6)$ bending mode, the ^5A_g ground term is stabilized in the $\phi_{\nu 2} \sim 0°$ geometry. In Figure 11 is shown the energy of the ^5A_g ground term of $[Mn(OH_2)_6]^{3+}$ as a function of $\phi_{\nu 5}$, calculated using the AOM. $\rho_{\nu 5}$ is set to the experimental value 0.89°, and the AOM parameters, given in the caption, are chosen so as to mimic the effect of the observed tetragonal distortion (see figure caption for the parameters used). One minimum is found at

---

(63) Prager, M.; Heidemann, A. *Chem. Rev.* **1997**, *97*, 2933.

$\phi_{\nu 5} \sim 164°$. The experimental value is 142(15)°, and this is superimposed on the figure. The variation of the energy of the ground state as a function of displacement along $\tau[M(OH_2)_6]$ was not considered as ρ_τ is only just significant and ϕ_τ is poorly defined.

The quantity $\rho_{\nu 2}$, as calculated from the crystallographic positional parameters, $\rho_{\nu 2}$ (cpp), is sometimes referred to as the Jahn−Teller radius.[3,57,58,64] We have avoided using this term as we think it is misleading. The Jahn−Teller radius, R_{JT}, corresponds to the value of $\rho_{\nu 2}$ where the energy of the molecule is a minimum. This is not the same as the value of $\rho_{\nu 2}$ (cpp), which reflects the mean values of the atomic coordinates; $\rho_{\nu 2}$ (cpp) approaches R_{JT} at sufficiently low temperatures when the system is subject to a low-symmetry strain of sufficient magnitude to localize the ground state in one of the three minima. At 170 K, $\rho_{\nu 2}$ (cpp) = 0 for the $[Mn(OH_2)_6]^{3+}$ complex; the Jahn−Teller effect is not suppressed, as suggested;[42] the true minimum lies farther out along the $\nu_2(MO_6)$ coordinate; overall S_6 symmetry is preserved by dynamical averaging between the equivalent, tetragonally distorted structures.[50] R_{JT} can be estimated from the thermal parameters, as described in ref 2. Inspection of the cubic phase fractional coordinates and thermal parameters for CsMnSD, CsTiSD, CsGaSD, and CsVSD (see Supporting Information) shows that, in all cases, the metal(III)−oxygen bond vector is closely aligned with the X axis, and the anisotropic thermal parameters B_{13} and B_{12} for the O(b) atom are close to zero. The mean-square amplitude of O(b) along the Mn−O bond vector is then, to a good approximation, given by the parameter B_{11}. It follows that the mean-square displacement pertaining to the metal(III)−oxygen stretching motion is

$$\langle \Delta d^2 \rangle = \frac{B_{11}(\mathrm{O(b)}) - B_{\mathrm{iso}}(\mathrm{metal(III)})}{8\pi^2}\ \text{Å}^2 \qquad (11)$$

where the quantity $\langle \Delta d^2 \rangle$ is composed of contributions from all the metal−oxygen stretching vibrations. For CsTiSD, CsGaSD, and CsVSD $\langle \Delta d^2 \rangle \approx 0$, whereas for CsMnSD, $\langle \Delta d^2 \rangle = 0.0081(10)$ Å^2. A rough estimate of R_{JT} can be obtained by setting $\langle \Delta d^2 \rangle$ to the quantity $(r_i - r_{av})^2$ in eq 4, in which case $R_{JT} \sim 0.22$ Å, in good agreement with the value estimated from the 5 K structural data ($\rho_{\nu 2} = 0.234(2)$ Å).

The quantity R_{JT}, along with the Jahn−Teller stabilization energy E_{JT}, and the barrier height between the Jahn−Teller minima 2β, have been calculated by Daul and co-workers for the $[Cu\{(NH_3)_2sar\}]^{4+}$ complex (sar = 3,6,10,13,16,19-hexaazabicyclo[6.6.6]icosane) using the DFT method.[58] The calculated value of $4E_{JT}$ was found to be in excellent agreement with optical absorption measurements, whereas the calculated value of R_{JT} far exceeds the value of $\rho_{\nu 2}$ (cpp) calculated from a room temperature structure; attributed, rather unconvincingly, to a "restricted Jahn−Teller distortion imposed by the cage". In this instance the results of the DFT calculations are, in fact, better than the authors will have us believe. There is no discrepancy as such; but, the calculated value of R_{JT} should be compared to $\rho_{\nu 2}$ (cpp) calculated from a low-temperature structure.

The quantities E_0 and 2α obtained from fitting the calculated points in Figure 9a should not be confused with E_{JT} and 2β as usually defined.[50] We have simply fixed $\rho_{\nu 2}$ at the experimental value and calculated the energy of the molecule as a function of $\phi_{\nu 2}$. The path of minimum energy will in fact vary with $\rho_{\nu 2}$ due to higher-order effects.[50] We have, in addition, undertaken DFT calculations to estimate R_{JT}, E_{JT}, and 2β, using a procedure similar to that outlined for the VCl_4 and $[Cu(en)_3]^{2+}$ complexes.[57,58] Notwithstanding that the results are unlikely to enter into the ever growing annals of *the edification of chemists courtesy of DFT*, some comment would be appropriate at this juncture. Maintaining the average Mn−O bond distance at the value determined at 5 K, and optimizing the O−H bond lengths for each point, a value of $R_{JT} = 0.166$ (3) Å is obtained, which is far short of the value of $\rho_{\nu 2} = 0.234(2)$ Å determined at 5 K. In addition, the value of $4E_{JT}$ is approximately half that estimated from the optical data.[65] However, as the average Mn−O bond length is allowed to increase beyond the experimental value, so do R_{JT} and E_{JT}. It is here that DFT contributes to one's chemical erudition, as the series of calculations demonstrates a clear trend, providing insight into the displacement along $\nu_1(MnO_6)$ on cooling from 170 down to 5 K ($\rho_{\nu 1} = 0.014(2)$ Å). The results suggest that a displacement along $\nu_1(MnO_6)$ in turn affords a larger displacement along $\nu_2(MnO_6)$; the $[Mn(OH_2)_6]^{3+}$ complex in the alum is best described as an $E\otimes(e\oplus a)$ Jahn−Teller coupled system. The application of ab initio calculations to understanding the intricacies of metal-water bonding interactions, in the solid state, is clearly limited. Future work should be directed toward extending the basis set to include the environment about the aqua ion under consideration. The quantitative agreement between the calculations of Daul and co-workers and optical data on the $[Cu(en)_3]^{2+}$ and $[Cu\{(NH_3)_2sar\}]^{4+}$ cations is certainly impressive,[58] this being obtained by performing a full geometry optimization; but the calculated average Cu−N bond distance is larger than the experimental values, the degree of discrepancy being dependent upon the functional employed.

5. Conclusion

In the foregoing analysis, we have sought to prevail upon the reader the need to undertake a careful mathematical examination of the changes in the atomic positional parameters, which arise from structural phase transitions. The displacements of the $[Ti(OH_2)_6]^{3+}$ and $[Mn(OH_2)_6]^{3+}$ cations along the stretching, bending, and twisting internal coordinates, depicted in Figure 5, have each been quantified in terms of a vector of magnitude ρ, and angle ϕ, in the corresponding two-dimensional coordinate subspaces. The ground term of the $[Mn(OH_2)_6]^{3+}$ cation is, as expected, strongly coupled to the $\nu_2(MnO_6)$ vibration; but, the small

---

[64] Rauw, W.; Ahsbahs, H.; Hitchman, M. A.; Lukin, S.; Reinen, D.; Schultz, A. J.; Simmons, C. J.; Stratemeier, H. *Inorg. Chem.* **1996**, *35*, 1902.

[65] Johnson, D. A.; Nelson, P. G. *Inorg. Chem.* **1999**, *38*, 4949.

displacement along the $\nu_5(MO_6)$ bending mode is found to contribute to the localization of the $[Mn(OH_2)_6]^{3+}$ cation in one of the otherwise three equivalent minima on the $\nu_2(MnO_6)$ potential energy surface. That the $[Ti(OH_2)_6]^{3+}$ cation is not consumed with equal ardor to distort along the $\nu_2(MO_6)$ coordinate will not come as a surprise to chemists acquainted with the rudiments of bonding in transition metal complexes. The t_{2g} orbitals are not involved in σ-bonding, and hence their energies are rather insensitive to Ti−O bond length changes. However, the t_{2g} orbitals are weakly π-antibonding, and the π-bonding in the complex is perturbed by changes in the O−Ti−O bond angles and in the disposition of the water molecules about the Ti(III) cation. It is for this reason that the displacements along the e_g components of the $\nu_5(MO_6)$ and $\tau[M(OH_2)_6]$ modes are far greater for $[Ti(OH_2)_6]^{3+}$ compared to $[Mn(OH_2)_6]^{3+}$. For the given values of ρ, the AOM calculations for the $[Ti(OH_2)_6]^{3+}$ cation suggest that the associated values of ϕ are such as to maximize the stabilization of the ground state. Given the constraints imposed by hydrogen bonding, it seems a remarkable feat of nature that the structural changes that accompany the 13 K phase transition of CsTiSD can locate the aqua ion at the minimum of the multidimensional Jahn−Teller potential energy surface, and facilitate the transmission of long-range order.

We would like to emphasize that the variations in the structural chemistry of the β-alums can be adequately explained by elementary AOM calculations. Previous attempts to rationalize structural anomalies, from considerations of orbital overlap,[44] have been questioned in the light of “more sophisticated” ab initio calculations.[42,43] In particular, “DFT” has been fashioned into a shibboleth by its votaries. Notwithstanding the tremendous advances that have been made in theoretical inorganic chemistry,[66] caution should always be applied when rationalizing solid-state phenomena on the basis of ab initio gas-phase calculations alone.

Although we would not claim that the alum crystal system constitutes a viable model for a biological water oxidation center;[67] structural,[13] spectroscopic,[39] and magnetochemical[46] studies of these salts have provided unrivalled perspicacity concerning the correlation between electronic and molecular structure, a fundamental area of research that is central to understanding chemical processes.

Acknowledgment. We thank Hans-Beat Bürgi for very stimulating discussions, particularly with regard to the interpretation of the temperature factors. This work was funded by the Swiss National Science Foundation.

Supporting Information Available: Tables of fractional coordinates, thermal parameters, collection and analysis parameters, and selected interatomic bond lengths and bond angles. This material is available free of charge via the Internet at http://pubs.acs.org.

IC0259639

---

(66) Deeth, R. J. Computational Modelling of Transition-Metal Centres. *Struct. Bonding* **1995**, *82*, 1−42. Chermette, H. Density functional theory−A powerful tool for theoretical studies in co-ordination chemistry. *Coord. Chem. Rev.* **1998**, *180*, 699−721.

(67) Andres, H.-P.; Bominaar, E. L.; Smith, J. M.; Eckert, N. A.; Holland, P. L.; Münck, E. *J. Am. Chem. Soc.* **2002**, *124*, 3012.